Comprehensive Inorganic Chemistry III

Local structure determination using total scattering data

Simon J. L. Billinge (orcid: 0000-0002-9734-4998)
Sandra H. Skjaervoe (orcid: 0000-0002-1532-2008)
Maxwell W. Terban (orcid: 0000-0002-7094-1266)
Songsheng Tao (orcid: 0000-0002-7565-3503)
Long Yang (orcid: 0000-0001-8731-0172)
Yevgeny Rakita (orcid: 0000-0003-0448-3735)
Benjamin A. Frandsen (orcid: 0000-0002-4047-9453)

July 9, 2021

Contents

1 Introduction **2**

2 Structural phase transitions **5**

3 Battery electrode materials under cycling **7**

4 Semiconductor nanoparticles **8**

5 Inorganic molecular cluster structures **10**

6 Soft inorganic structures: halide perovskites **11**

7 Metal-organic frameworks and host-guest systems **12**

8 Layered materials **17**

9 Polycrystalline thin films **18**

10 Amorphous systems **19**

11 Nucleation of crystallites **22**

12 Magnetic crystals **24**

13 Future development **26**

14 Acknowledgements **27**

1 Introduction

Atomic structure plays an important role in determining the properties of materials, and it is widely appreciated that a detailed knowledge of structure is needed to better understand or predict the properties. For crystalline materials, a starting point is the crystal structure, obtained using crystallographic methods that exploit the diffractive nature of crystals to short wavelength radiation. This is the periodically averaged view of the material structure and, whilst enormously valuable, is an idealization of the real situation. We are increasingly learning to appreciate the often significant roles in a material's functionality played by various imperfections or deviations from these idealized models, not to mention the countless materials that do not play by the same rules of periodicity such as nano- and amorphous materials. Thus, further insights are often required, beyond the perfectly-ordered, model structures (Figure 1a,b). In this chapter we describe the atomic pair distribution function (PDF) analysis of total scattering powder diffraction data as an approach to gain insight into the real structure of materials. What we mean by real structure is the atomic arrangement taking into account defects, structural relaxations around those defects, morphology, structural coherence and so on. We can delve deeper by using total scattering methods.

Total scattering measurements are very similar to conventional diffraction measurements. What makes them "total" is that they take into account all the information in the scattering pattern, even the diffuse signals in-between (and underneath) the Bragg peaks. This includes the diffraction intensities coming from the periodic structure giving rise to Bragg peaks (the global, or average, structure, Figure 1b), elastic diffuse scattering (the static local structure, Figure 1c), and inelastic diffuse scattering from moving atoms that contain information about dynamics [1] (Figure 1e). To harvest the structural information as completely as possible, measurements require as wide a range of reciprocal space as possible (corresponding to smaller d-spacing resolution), which require shorter wavelengths and higher fluxes of x-rays, neutrons, or electrons. The techniques have come into their own with increases in short wavelength flux at neutron spallation sources and x-ray synchrotrons (Figure 1a) and improvements in transmission electron microscopes, which allow weak diffuse signals to be more accurately measured. Finally, with the advent of powerful computers and advanced software, the somewhat computationally intensive analysis has become straightforward and user-friendly, leading to a massive growth in the application of these methods [2].

A practical, powerful, and often intuitive way to analyze total scattering data is to Fourier transform the reciprocal space scattering function $S(Q)$ to real space to obtain the PDF, $G(r)$. The PDF is basically a histogram of inter-atomic distances, spatially and temporally averaged over the entire sample (Fig. 1c and g). The peak positions indicate that pairs of atoms are separated by said distance; the intensity reflects the number of pairs and scattering power of constituent atoms, and the width represents the variation of a specific pair distance due to thermal motion or disorder. Processes such as atomic relaxation, displacement, or dynamic correlation affect the PDF peaks differently, leading to splitting, changes in shape, sharpening and so on. The information found in the low-r region of the PDF is directly related to the short- and mid-range local arrangements of atoms, regardless of the long-range order. Assessing this information requires that we approach the data analysis a bit differently than for crystallographic structure solution from reciprocal space. A crystallographer's goal is to determine the periodic arrangement of atomic motifs, which requires using the highest possible symmetry that fits the diffraction pattern [3]. In a PDF analysis, we are often interested in determining how the local structure can deviate from these high-symmetry descriptions, or even determining some details of the local structure in cases where we cannot so readily determine an 'average' model [1].

When analysing the PDF, we often start by evaluating the data in a model-independent way. Our ability to understand intuitively what the PDF peaks mean enables us to learn a lot about a material by simply looking at the peaks. Using intuition about bonds and structural degrees

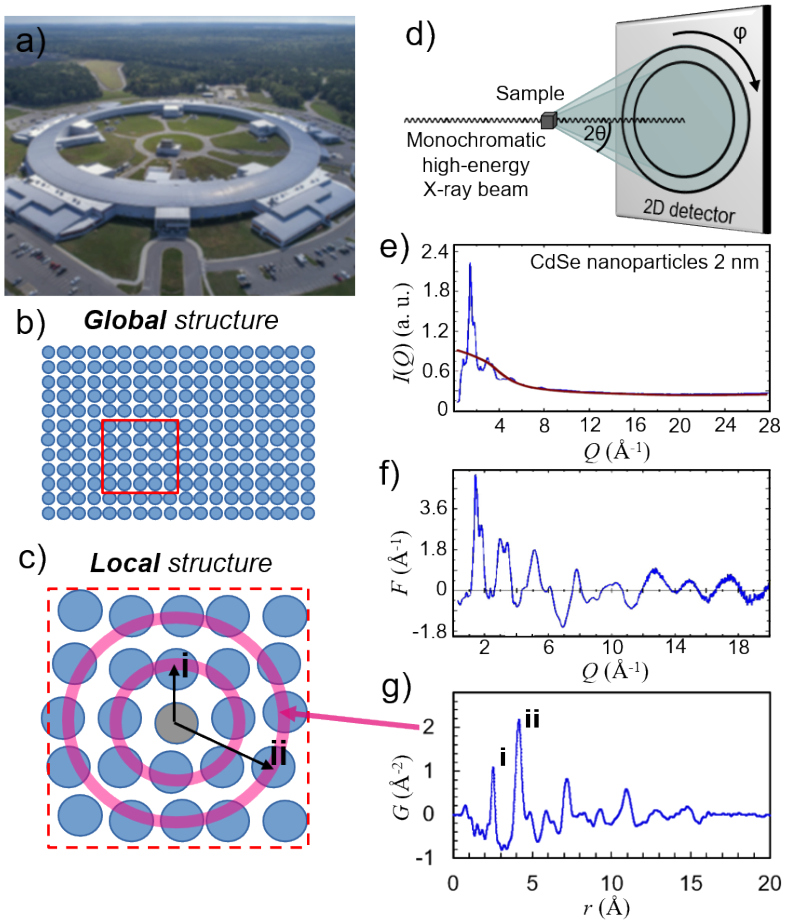

Figure 1: a) Aerial photo of NSLS II at Brookhaven National laboratory on Long Island, NY, as state-of-the-art x-ray synchrotron facility. b) Sketch of a highly crystalline global structure, the way one might imagine it looks like with assessment by conventional Bragg diffraction analysis, as this probes only the periodic component of the structure. c) Close up of an excerpt of the structure sketch above, where the atoms are now randomly displaced out of the high-symmetry positions. This might not lead to a global lowering of the symmetry, since the displacements cancel out, but locally, it can have great implications. d) Sketch of the experimental setup showing monochromatic x-rays with high energy scattering off the sample to form bright rings for angles 2θ, (2theta), where the Bragg condition is fulfilled. e) An example of a measured scattering intensity $I(Q)$, here for a sample of CdSe nanoparticles where the red line highlights the diffuse scattering, f) the corrected reduced scattering function $F(Q)$ and g) the pair distribution function $G(r)$. The pink arrow pointing to the circles in panel c) illustrates the link between the coordination environment around each atom and the peaks of the PDF. (e)-(f) where reprinted with permission from ref. [2].

of freedom we can build a structural model to fit the data that goes beyond the global crystal symmetry. These models can be as small as a single molecule or cluster, a crystallographic unit cell, or larger depending on how many degrees of freedom one wants to allow. Since local chemical bonding is imperative for the mechanisms that cause symmetry to break, the inorganic chemist's real-space bonding perspective is of great advantage when it comes to PDF analysis. In this chapter we will explore a number of different situations which serve to exemplify the kind of chemical and structural scenarios where total scattering and PDF can add significant value, as well as giving hints at how the PDF analysis was done to extract the information. More details can be obtained by reading the original papers referenced. A slightly technical reference book for the technique is [1], and a more gentle introduction to the method can be found in [4]. For visual clarification of the formalisms of total scattering, see [5]. For more about the implications of using neutrons for obtaining the PDF, see [6].

Total scattering measurements

Total scattering measurements are typically performed on powder samples, just like in an in-house powder diffractometer. When doing a total scattering measurement we are obtaining the scattered intensity in a large portion of the reciprocal space, and we typically need synchrotron x-rays or spallation neutrons with high enough intensity to achieve that. Anyone can apply for beamtime to perform specific experiments for free by submitting an application to the facilities' websites. The facilities are divided into several beamlines, all with their own specialized expertise, experimental setups, and sample environments. Reaching out to the beamline scientist in advance of a proposal will increase the chances of a proposal being accepted, since one is better equipped to tailor the proposal to the specific beamline's expertise and interests.

Formal description of the PDF

The coherent signal that is scattered out of the sample is referred to as the scattering intensity $I(Q)$, derived in 1915 by Pieter Debye [7],

$$I_{coh}(Q) = \sum_i \sum_j f_i(Q) f_j(Q) \frac{\sin(Qr_{ij})}{Qr_{ij}} \tag{1}$$

where $f_i(Q)$ and $f_j(Q)$ are form factors for the atoms i and j separated by r_{ij} and Q is the reciprocal space distance. The acquisition of the scattering intensity can be done rapidly using a 2D detector, where the scattering from the sample forms bright rings where the Bragg condition is fulfilled.

In order to get the pair distribution function $G(r)$ from the data we first need to integrate over the azimuthal angle (Figure 1d) of the 2D pattern, obtaining the 1D function $I(Q)$, illustrated in the top panel of Figure 1e). The next step is removing contributions from parasitic scattering, such as background, Compton scattering, absorption and fluorescence, resulting in the coherent intensity, $I_{coh}(Q)$, that can be converted to the total scattering structure function $S(Q)$ according to

$$S(Q) = \frac{1}{N\langle f \rangle^2}[I_{coh}(Q) + \langle f \rangle^2 - \langle f^2 \rangle], \tag{2}$$

where N is the number of scatterers and f is the atomic form factor. The final step is to Fourier transform the reduced scattering function $F(Q) = Q[S(Q) - 1]$ (Figure 1f), which gives the pair

distribution function $G(r)$ (Figure 1g), defined as [1]

$$G(r) = 4\pi r[\rho(r) - \rho_0], \tag{3}$$

where $\rho(r)$ is the atomic pair density and ρ_0 is the average number density.

While these steps are somewhat advanced, there are several tools available that simplify the process, such a PDFgetX3 [8], PDFgetN [9], PDFgetN3 [10], GSAS-II [11], TOPAS [12], GudrunX and GudrunN [13]. The analysis of $G(r)$ can finally be done using easy-to-use software, such as PDFgui [14] and TOPAS [12].

2 Structural phase transitions

Many of the materials we use undergo structural phase transitions that bring about the very properties we use them for. A good example is that of ferroelectric materials: dielectric crystalline materials that form a switchable spontaneous electric polarization below a critical temperature, while no polarization can be measured above. These materials have applications in capacitors, data storage and sensors, among many others.

The changes in the long-range symmetry of the crystal brought about by the phase transition can be seen crystallographically. The local point of view, however, is often overlooked. In some cases this has led to incomplete and incoherent descriptions of a material's properties.

A "classic" example of this is the ferroelectric $BaTiO_3$, which goes through a series of phase transitions where the electric polarization changes direction as the symmetry is lowered. At high temperatures, the structure has cubic symmetry and no electric polarization. On cooling, the symmetry breaks to tetragonal, then to orthorhombic, and finally to rhombohedral, all three accompanied by the emergence of an electric polarization in the direction of the long-axis of the respective crystal structure. The change in symmetry and polarization direction were originally believed to be due to a collective displacement of the Ti atoms inside the octahedra in the direction defined by the distortion of the unit cell. However, PDF analysis revealed that the Ti atoms were always, in all phases at all temperatures, displaced along the body diagonal of the cell, in the direction defined by the rhombohedral distortion seen at low temperatures. The crystallographic symmetry is therefore merely the average over different sets of local rhombohedral displacements [15, 16, 17]. This was among the first examples showing how understanding of the local structure can resolve conflicts between the average symmetry and physical properties, which can sometimes appear to be contradictory. For $BaTiO_3$ it meant that one could understand one of the reasons for its significantly lower polarization compared to its close relative $PbTiO_3$. PDFs have since been used to study phase transitions in a wide range of different materials. We mention in particular the confirmation of polar nanodomains in "relaxor" ferroelectrics[18, 19, 20, 21] and other related oxide perovskites [22, 23], local structural symmetry breaking at metal-insulator transitions[24, 25, 26], the link between structure and emergence of superconductivity [27, 28], the unusual symmetry breaking in the softer halide perovskites [29, 30], and the interplay between the magnetic ordering and incommensurate structural symmetry breaking in a hexagonal manganite [31].

In a recent study, the PDF technique was used to reconcile decades of seemingly anomalous observations across the structural phase transitions in the scientifically and technologically interesting multiferroic hexagonal manganite, $YMnO_3$ (Fig. 2a). The high temperature transition at 1250 K was already known to cause a symmetry breaking from the non-polar $P6_3/mmc$ to the polar $P6_3cm$, although any measurable polarization could not be found until a temperature several hundred degrees lower. Attempts at describing the mechanism of the phase transition with

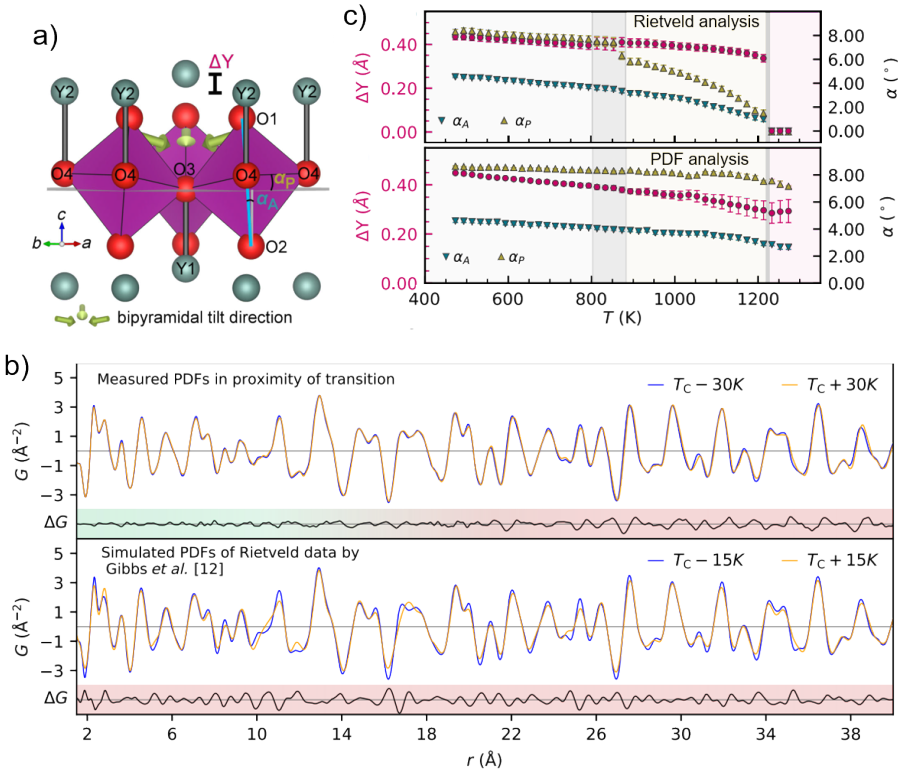

Figure 2: a) An excerpt of the hexagonal manganite structure in its polar ground state with $P6_3cm$ symmetry. Yttrium in green-blue, oxygen in red and manganese in trigonal bipyramids in purple. The excerpt emphasizes the connection between the corrugation δY of the Y atoms along c (distance in the c direction between Y1 and Y2) and the tilting of the Mn-O polyhedra, defined through the two tilt parameters α_A and α_P. Green arrows indicate the directions of the bipyramidal tilts. In the average structure at high temperature $\delta Y = \alpha_A = \alpha_P = 0$. b) Comparison of experimental (top) and simulated (bottom) PDFs for temperatures bracketing the structural transition at T_C. The simulated PDFs are calculated using the average structure information from previously reported Rietveld refinements [32] across the transition. Corresponding difference curves are shown underneath. The shaded green and red areas behind the difference curve indicate, respectively, regions of low and high difference. c) Comparison of resulting fitting parameters δY, α_A and α_P from Rietveld analysis of the reciprocal space data (top) and PDF analysis of the real space data (bottom). The Rietveld fitting was done with the polar ground state model below T_C (indicated by the gray vertical line at 1223 K), and the high-symmetry non-polar model above, as inferred from the Bragg reflections. The PDF data was fitted with the polar ground state model over the entire temperature range. Reproduced from [33].

Bragg diffraction proved inconclusive. The most glaring anomaly was that the atomic positions, as extracted from Rietveld analysis, seemed to make discontinuous jumps across the transition [32] - a sign pointing to a first-order transition - even though this was inconsistent with the smoothly evolving lattice constants [32] and heat capacity measurements [34]. In order to reconcile these apparent anomalies, Skjærvø *et al.* [33] performed high-temperature neutron PDF measurements on a powder sample for temperatures ranging from room temperature to above the transition. Neutrons allowed the signal from the Y and Mn to be distinguished, as Mn has a negative scattering length. The PDF analysis showed that the structure went through an order-disorder transition, evidenced by the lack of qualitative changes in the low-r data across the transition (Fig. 2b). Had the local symmetry breaking been consistent with the long-range order, the PDF would change qualitatively across the transition, as demonstrated in the lower panel of Fig. 2b. In other words, the local bonding environment stayed the same across the transition, leading to the conclusion that any loss in symmetry must be due to disordering. Instead of the discontinuous jumps in atomic positions observed for the average structure data, the PDF fits gave continuously changing values (Fig. 2c) that were far away from those associated with the high-symmetry phase. Interestingly, the study further suggested that this order-disorder mechanism was of a type not previously known, with the primary order parameter being able to rotate continuously over all angles upon approaching the transition from below. The discovery of this mechanism reconciled the anomalous diffraction data and macroscopic measurements.

3 Battery electrode materials under cycling

The efficiency of an electrochemical device such as a fuel cell or a battery depends heavily on the atomic composition, structure, and morphology of the materials making up the various components of the device - anode, cathode, electrolyte, and separators. Optimization relies on our ability to both understand the materials individually as well as their interaction with the other components as the device operates. Studies to probe the structure and morphology can be done on the individual components post-operation (*ex situ*), under relevant physical conditions in the beam (*in situ*), or even studying changes to the material directly in the beam in an operating device such as a cycling battery (*operando*).

Electrochemical processes cause dramatic structural changes in materials. To fully understand these changes we often need several scattering techniques. Conventional diffraction can tell us the changes in overall symmetry, order, crystallite size and phase composition; small-angle scattering can tell us about the particle size distribution, morphology, and texture. PDF is the ideal choice if we want to uncover details of short range effects and how they deviate from the global symmetry [36]. PDF has been used *ex situ* for studying Li intercalation in silicon anode materials [37]; atomic defects in Fe particles [38] and structural robustness of the cathode material [39] in conversion type cathodes made from Fe fluorides, oxides and oxyfluorides; *operando* local accommodation of sodium in phoshorous anodes [40] and of Li in Li-Fe-S cathodes [35]. PDF has also been used to study *operando* the local atomic changes in noble metal transition metal nanocatalysts during oxygen reduction reactions [41]. More recently, the development of 3D δ-PDF has proven useful for model independent studies of local structural changes by subtracting the Bragg signal. Being restricted to single crystals, the method was successfully applied to understand the ordering of sodium along the different crystallographic axes of the sodium-intercalated compound V_2O_5 [42].

In a study of Li accommodation in Li-Fe-S cathodes [35], PDF was combined with x-ray absorption spectroscopy and first-principles calculations to shed light on the formation of phases in the Li-Fe-S composition space during repeated charge-discharge cycles of the cathode. The study revealed a complex picture of intermediate phases during both charging and discharging, resembling

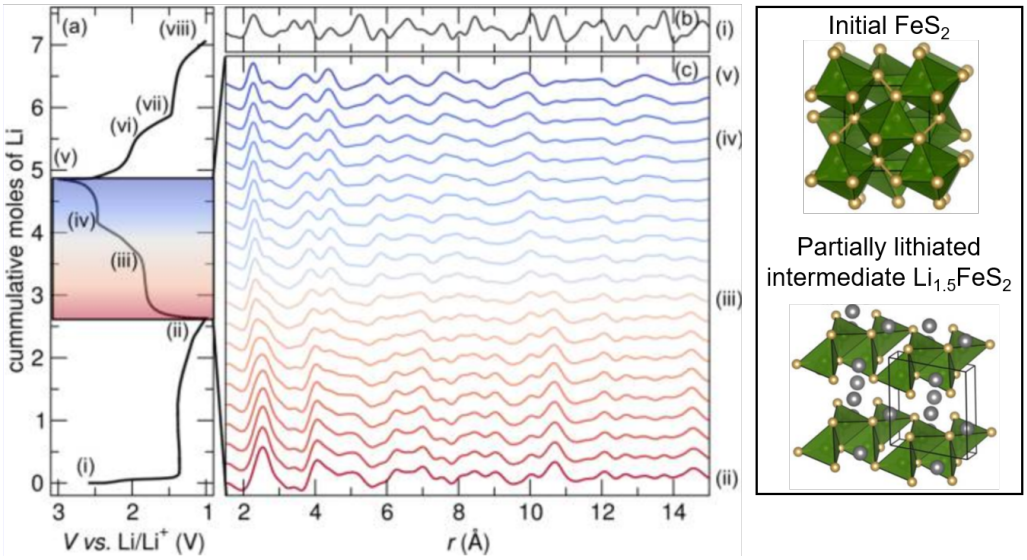

Figure 3: The effect of electrochemical cycling on the local structure during the first 1.5 cycles of *operando* electrochemistry.(a) Amount of Li accumulated in the material as a function of voltage. (b) PDF of the as-prepared FeS_2 before cycling (see top right for structure). (c) PDFs showing the evolution of the local structure. The local structure evolves through partially lithiated phases where Fe is tetrahedrally coordinated (see bottom right image for example). The tetrahedral coordination differs significantly from the octahedral coordination in the original FeS_2 structure, which is never recovered during the cycling. Reproduced from [35]

.

mechanisms of intercalation rather than pure conversion, as shown in Fig. 3. Most interestingly, the initial structure of FeS_2 with octahedrally coordinated iron was never recovered during the cycling. Since the gradual evolution through partially lithiated intermediates for the most part do not lead to any changes in the long-range ordering of the material, the effects would not have been observable with conventional diffraction, thereby illustrating clearly the need for PDF in describing the structure.

4 Semiconductor nanoparticles

In recent years the characterisation of atomic structure in nanoparticles has become one of the main uses of PDF. Quantum dots (QDs), for example, CdSe nanoparticles (CdSe NPs) of a few nm diameter, are among the most important and the most studied of these. Unlike bulk materials, small nanoparticles do not give rise to sharp x-ray or neutron Bragg peaks, but instead, only broad, diffuse scattering features. The PDF method can add significant value in helping us to interpret these [43, 44]. QDs have unique optoelectronic properties coming from the size and internal structure of their inorganic cores as well as the nature of the passivating ligand shell and it is important to understand factors such as defects, surface relaxations and internal strains, as well as the average internal arrangement of atoms in the core. There are many excellent studies of QD structures using PDF [45, 46, 47, 48, 49, 50].

Surprising progress can be made by taking simple modeling approaches. This requires some creativity in designing models and modelling approaches, and the best way of doing this is highly

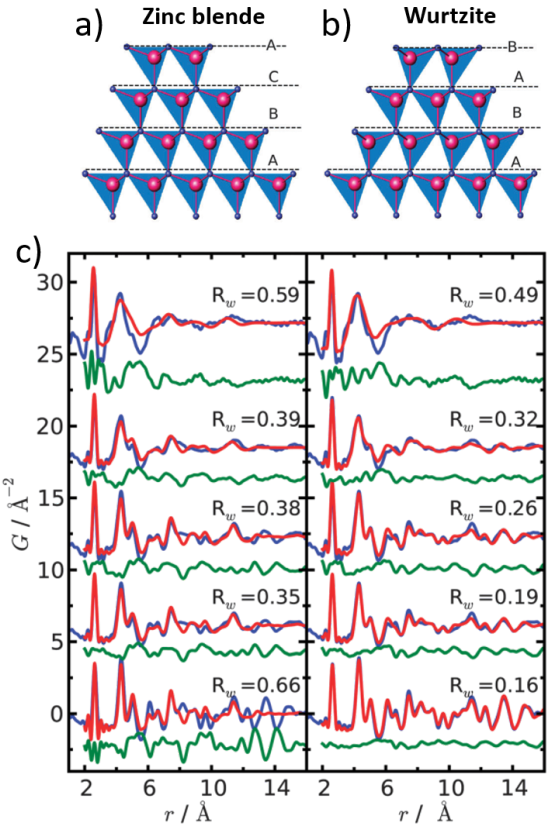

Figure 4: Layer stacking sequences of the two closely related zinc blende (a) and wurtzite (b) structures, with A, B and C denoting the difference in the stacking type. c) Measured PDF for CdSe nanoparticles of various sizes, with small nanoparticles of 13 nm at the top and bulk-sized particles at the bottom. The fitting residual R_w is given next to the curves. The wurtzite structure gives consistently better fit than then zinc blende structure, even for the smallest particles, as seen from the R_w values. Reproduced from [46].

dependent on the system in question. For example, in the case of CdSe quantum dots, there is particular interest in the relationship between size and structure [45, 46]. Bulk CdSe generally takes the *wurtzite* crystal structure. A cutout of the structure is illustrated in Figure 4 along with its sister structure *zinc blende*. In the wurtzite structure, the anions sit in a hexagonal closed packed (hcp) structure, while the cations are in the tetrahedral sites in the structure. In the closely related zinc blende structure, on the other hand, the anions form a cubic closed packed (ccp) structure with the cations in the tetrahedral sites. The difference between the hcp and ccp structures can be understood in terms of atom layering: the atomic layers in the wurtzite (hcp) structure can be described as an ABABAB stacking, while the layer stacking in the zinc blende (ccp) structure is ABCABC. Layered structures like CdSe are prone to stacking faults, where the layering does not follow either ABABAB or ABCABC though the whole structure, but may have other sequences. PDF was able to show that stacking faults were important in CdSe NPs and to characterize the stacking fault density [45, 46]. In this modeling, which used the program PDFgui, a strategy was used where a bulk crystal structure was used for the starting model which was modified to explain the finite size of the particles by attenuating the PDF peaks with increasing r using a particular functional form, called the characteristic function, that encodes the particle size and shape. The PDF was also able to show that a spontaneous size-dependent compressive strain appeared in the

QDs as they got very small, both a small reduction in the average Cd-Se bond-length, and a small broadening of the PDF peak associated with that bond indicated a heterogeneous strain (different bond lengths in different parts of the sample) [46]. To learn more about factors such as defects, surface relaxations and differences in bond lengths between the center and edge of the nanoparticles, it is necessary to build explicit cut-out models of the nanoparticles and modify them as desired. This is not possible with PDFgui but can be done with other programs such as diffpy-CMI [51] and DISCUS [52, 53].

Beyond QDs, PDF studies are also numerous on metallic nanoparticles [54, 55, 56, 57, 58, 59, 60, 61, 62]. To make the study of such systems easier, Banerjee *et al.* [60] recently demonstrated that a high throughput data-mining approach could be used to screen large numbers of models (thousands) from different families of cluster motifs, which will make PDF studies on metallic nanoparticles more straightforward in the future. The *cluster-mining* capability will be deployed on the PDFitc.com [63] cloud platform in the future.

When clusters are sufficiently small they can have unique (atomically precise) structures and it makes sense to attempt to solve the structure exactly. This was done on 102 atom gold atom clusters using the techniques of protein crystallography [64]. However, nanoparticle structures have also been solved *ab initio* from PDF [65, 66, 67]. Single particle electron microscopy approaches also look promising in this regard [68]. We expect PDF studies of discrete nanoparticles to remain an important area of research for the foreseeable future.

5 Inorganic molecular cluster structures

Materials consisting of even smaller building blocks than the nanoparticles in the previous sections can exhibit extraordinary electronic properties beyond those found for the bulk version. Such ultra-small building blocks have been named clusters or superatoms [69, 70]. The cobalt chalcogenides have been successfully built into diatomic and triatomic superatom molecules [71], which have attracted considerable attention because of their potential applications in solar cells [72], electrocatalysis [73], and lithium-ion batteries [74].

In a recent work [75], a new solution-phase chemical approach was developed to dissociate the capping ligands from the molecular cluster $Co_6Se_8(PEt_3)_6$ using elemental Se as a phosphine scavenger. The high surface-to-volume ratio of the resulting Co-Se microspheres (CoSe-MS) make them promising materials for electrochemical devices, such as Na and Li ion batteries.

The structures of the CoSe-MS clusters are good candidates for study with x-ray PDF. However, due to the large phase space of possible cobalt selenium structures, manual fitting to a wide range of models would be a tedious job. To simplify this type of job, Yang *et al.* [76] recently developed the *structure-mining* approach to find the best-fit candidate structures from PDF data in a highly automated way. This approach (available on *PDF in the cloud* (PDFitc), https://pdfitc.org, see Fig. 5 [63]) fetches, from structural databases, all the structures meeting the experimenter's search criteria, and performs structure refinements on them without human intervention.

In the study of the Co-Se nanoclusters, the *structure-mining* searched for all the structures containing Co and Se with any stoichiometry, returning the nanocrystalline Co_3Se_4 (NC-Co_3Se_4) as the best fit (Fig. 6(a) inset). A closer inspection of the fit (Fig. 6(a)) suggested that even though this single-phase model fit the PDF peaks well in the high-r region, additional unfitted signal was evident in the difference curve in the low-r region. The authors improved the model by invoking a second phase with a significantly shorter structural coherence, as shown in Fig. 6(b), indicating that the material consists of short-range-ordered (SRO) and longer-range-ordered (LRO) Co_3Se_4 nanoclusters.

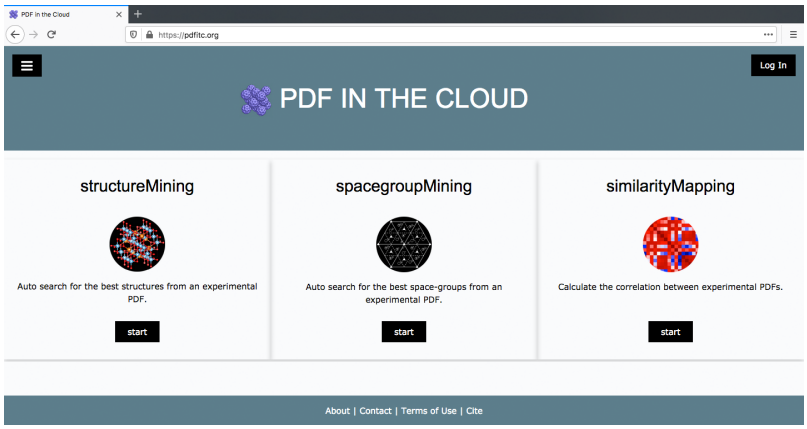

Figure 5: The home web page of PDFitc. Reproduced from [63] with permission of the International Union of Crystallography.

6 Soft inorganic structures: halide perovskites

Unlike regular (oxide) perovskites, Halide Perovskites (HaP) are ABX_3 structures with X being a halide, and A and B being mono- and di-valent cations, respectively. In recent years HaP, those with A as methylammonium, formamidinium or Cs, B being Pb or Sn, and X being Br or I, have caught the attention of the scientific community due to their outstanding opto-electronic performance in photovoltaics, LED, and radiation detection applications [77, 78, 79]. Structural imperfections, which normally inhibit carrier mobilities and introduce recombination pathways for photo-generated carriers are, surprisingly, found to have only a benign effect on HaPs with a small impact on device performance. This is in sharp contrast to the detrimental effects of analogous imperfections in classical semi-conductors, such as Si or GaAs [80, 81]. Evidence for self-healing [82], low formation energy with respect to their binaries [83] and low mechanical stiffness [84], and thermodynamic theory and modelling of point defects [85, 86] suggested that the structure is dynamic in nature. This has indeed been experimentally corroborated by studies using PDF [30, 87, 88], Raman [89] and IR [90] spectroscopies.

Generally, materials with a soft backbone will have a higher tendency to possess multiple local distortions, which will tend to average out into a high-symmetry representation due to the same reason. Because PDF measures the instantaneous structure, it is capable of studying the local broken symmetries even when they are fluctuating as dynamic disorder [30, 88].

For example, $CH_3NH_3PbI_3$ grown from solution was observed in conventional diffraction to have a perfect cubic perovskite-like structure above 330 K, but with a highly dynamic MA group [91, 92]. A closer look at the total scattering revealed a picture that is much less symmetric at short-range [30]. Fig. 7 shows that the calculated structural distortions, which are coupled to the $CH_3NH_3^+$ motion, result in anharmonic shallow double well-potentials, which are directly observed using PDF. By fitting different symmetry models to the PDF, over different ranges of r, the local and long-range structure could be differentiated. The long-range structure is clearly well fit with the cubic model, while the short/mid-range structure was best fit by tetragonal models with a preference towards the non-centrosymmetric one [30].

Combining the the real space PDF analysis with a reciprocal space analysis via the Debye Scattering Equation (DSE) (1), results in an accurate way to study nanoscale structural domains. The DSE approach extracts nanostructural information by detailed modeling of high Q-resolution

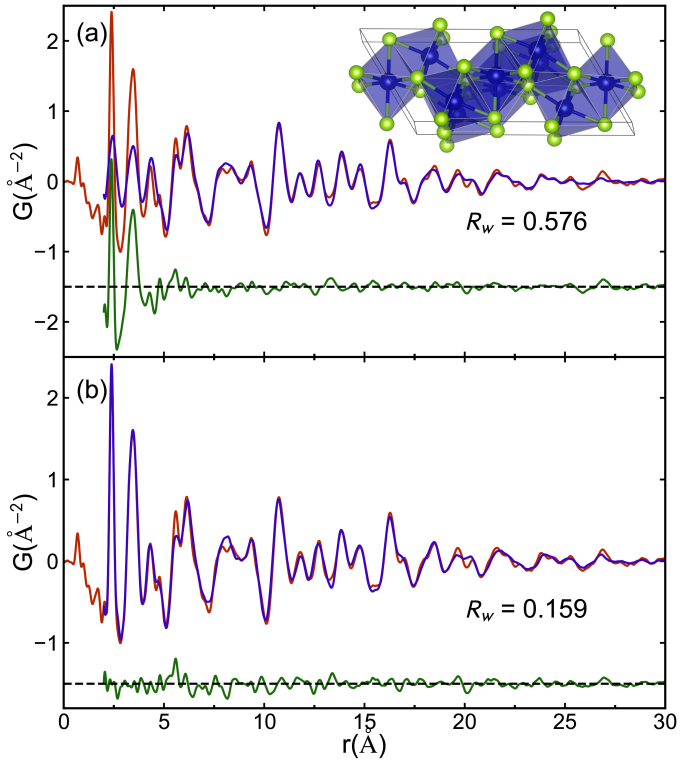

Figure 6: Measured x-ray PDF from the CoSe-MS (light red curve) with (a) the best-fit calculated PDF (purple) for the NC-Co_3Se_4 model. The model was fit over a range of $5 < r < 30$ Å but the plot shows the calculated curve extended to low-r. (b) the best-fit calculated PDF (purple) for the two-phase (SRO + LRO NC-Co_3Se_4) model. The fit was performed over a range of $2 < r < 30$ Å. The difference curves are shown offset below (green). R_w is the goodness of fit. The inset in (a) is the NC-Co_3Se_4 structure, where Co atoms are in blue, Se atoms are in green and octahedra are emphasized in shaded blue. Adapted with permission from [75]. Copyright 2019 American Chemical Society.

diffraction peak line-shapes, which complements the low-Q resolution, high r-resolution, PDF measures of the local structure. This combined approach was used with great success in the HaP to reveal nanoscale microstructure [93]. Using $CsPbX_3$ nanocrystals, Bertolotti *et al.* used a joint DSE/PDF approach to show that $CsPbX_3$ nanocrystals form orthorhombic sub-domains (occurring both in the room and high-temperature phases) hinged through a two-dimensional (2D) or three-dimensional (3D) network of twin boundaries across which the coherence of the Pb sub-lattice is preserved throughout the whole nanocrystal as shown in Fig.8. The density of these twin boundaries determines the size of the sub-domains and results in an apparent higher-symmetry structure on average in the high-temperature modification.

7 Metal-organic frameworks and host-guest systems

The term metal–organic framework (MOF) arose in the 1990s for a subclass of coordination compounds, typically considered to require crystallinity and ordered microporosity, although, this definition overlooks various types of structural disorder that are commonly observed in these materials.

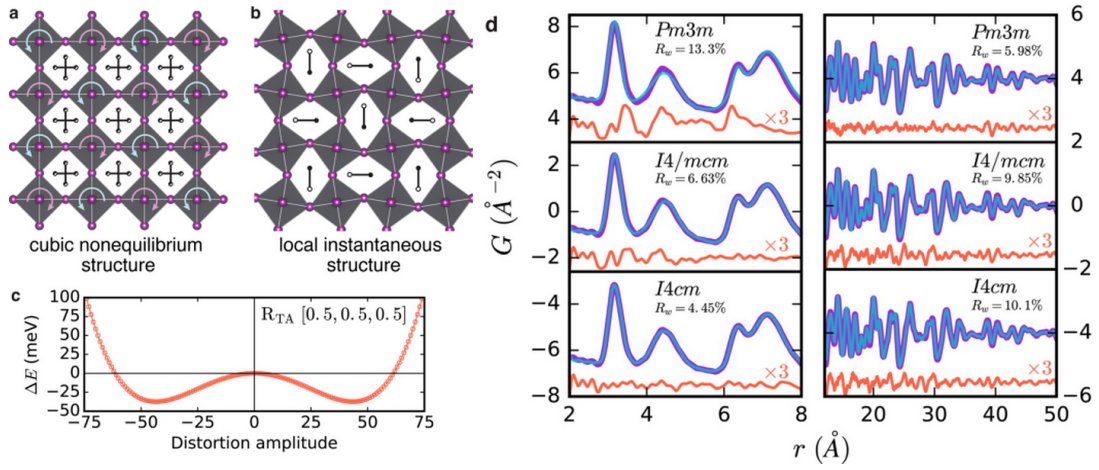

Figure 7: Local symmetry breaking in $CH_3NH_3PbI_3$ at 350 K. (a,b) Distortions from cubic symmetry and coupling to motion of the $CH_3NH_3^+$ ion. (c) DFT-based lattice dynamic calculations show that the energy minimum at the R point for 350 K is displaced to give a double-well potential that causes local symmetry breaking. (d) Comparison of the experimental PDF (purple) to cubic ($Pm\bar{3}m$), centrosymmetric ($I4/mcm$), and noncentrosymmetric ($I4cm$) tetragonal models (blue) shows a superior fit for the low-symmetry models at low r (2–8 Å). At high r (12–50 Å), however, the models perform oppositely, with the high-symmetry cubic structure giving the best agreement to the data. The residuals (orange) are scaled for clarity. Reproduced from [30].

The distinct sub-components comprising the frameworks, metal-ion or cluster nodes connected by organic linkers, result in non-typical structural degrees of freedom that can enable a rich diversity of defects and disorder in their formation. These can include the orientation and coordination of inorganic nodes, flexibility of the organic linker conformations, and the possibility for occupancy disorder [94]. Such properties are implicated for example in the phenomenon of breathing modes [95], interaction with adsorbed chemical species [96], negative thermal expansion [97], and even amorphization [98, 99].

Local structure studies of amorphous MOFs are difficult, and the number of well-characterized states is relatively limited. The first detailed structural investigation was presented by [98] on the structure of amorphized zeolitic imidazolate framework (a-ZIF) obtained by heating ZIF-4 up to 300 °C. The composition of the a-ZIF state could be constrained by the observation that it could be further transformed into a dense crystalline phase ZIF-zni on heating to 400 °C. While little information could be gleaned from the amorphous diffraction halo, both neutron and x-ray PDF measurements showed that the local structures of ZIF-4, a-ZIF, and ZIF-zni were nearly identical up to approximately 6 Å, Fig. 9(a,b), confirming the maintenance of tetrahedral coordination of Zn and bridging by imidazolate ions. A direct analogy to amorphous silica, where Zn replaces Si and imidazolate ions replace O, allowed for reverse Monte Carlo (RMC) refinements to be adapted, showing that a-ZIF forms with a continuous random network topology as shown in Fig. 9(c,d).

Products from different amorphization pathways have been further investigated with a focus on potential applications in sensors or encapsulation, for example, storage of radioactive agents [100] or even drug delivery [101]. PDF analysis has become a hallmark in the local structure characterization of these states. In cases where no crystalline analogue is formed, the confirmation of microporosity as well as successful incorporation and immobilization of reactive node species can be made by combination with theoretical calculations [102]. The survival of the chemical configuration, coordination, and porosity into a molten state has also been observed, leading to further

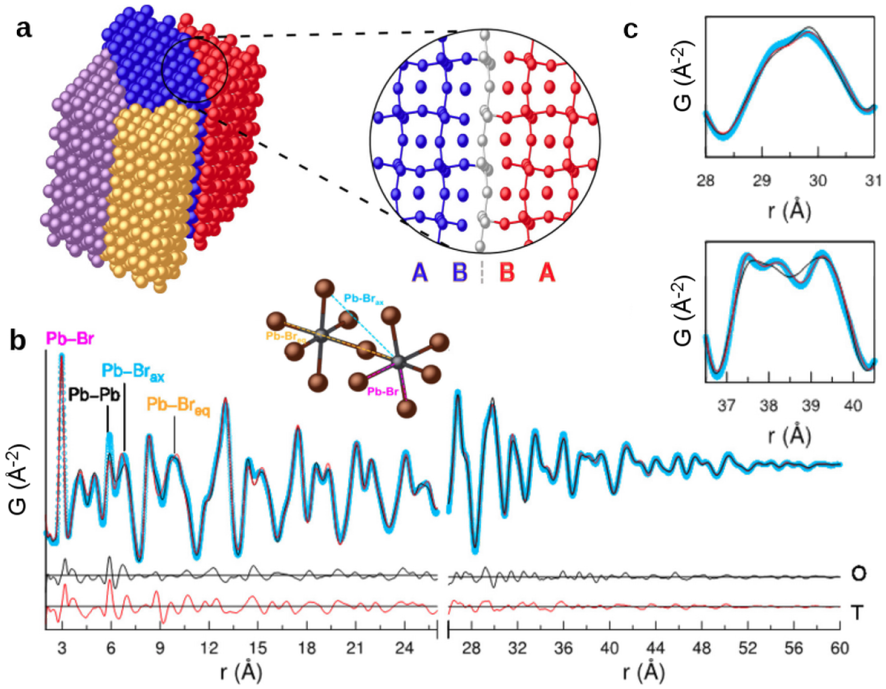

Figure 8: (a) Atomistic representation of nanotwins within a NC; the twin boundary highlighted in the circle shows the discontinuity of the halides lattice and the coherence of the Pb sublattice. (b) and an inset (c) are G(r) fits of RT $CsPbBr_3$ QDs: the black (red) solid lines show the residuals of the orthorhombic (tetragonal) model(s) in the low and medium r sections. The proposed orthorhombic structure fits significantly better (R_w = 12.9%) than the tetragonal structure (R_w = 18.5%). In the 26–70 Å range, however, a tetragonal structure is preferred (R_w = 10.9% vs 12.4%). The assignment of the marked peaks (Pb–Br, Pb $\cdots$ Br_{ax}, and Pb $\cdots$ Br_{eq}) is sketched in the inset (Pb, black; Br, brown). Interestingly, inter-octahedral Pb–Pb peaks in (b) are much narrower than expected, whereas Pb–Br peaks are broader, indicating a more ordered arrangement of the Pb network and the discontinuity of halide sub-lattice at the twin boundaries. Reproduced from [93].

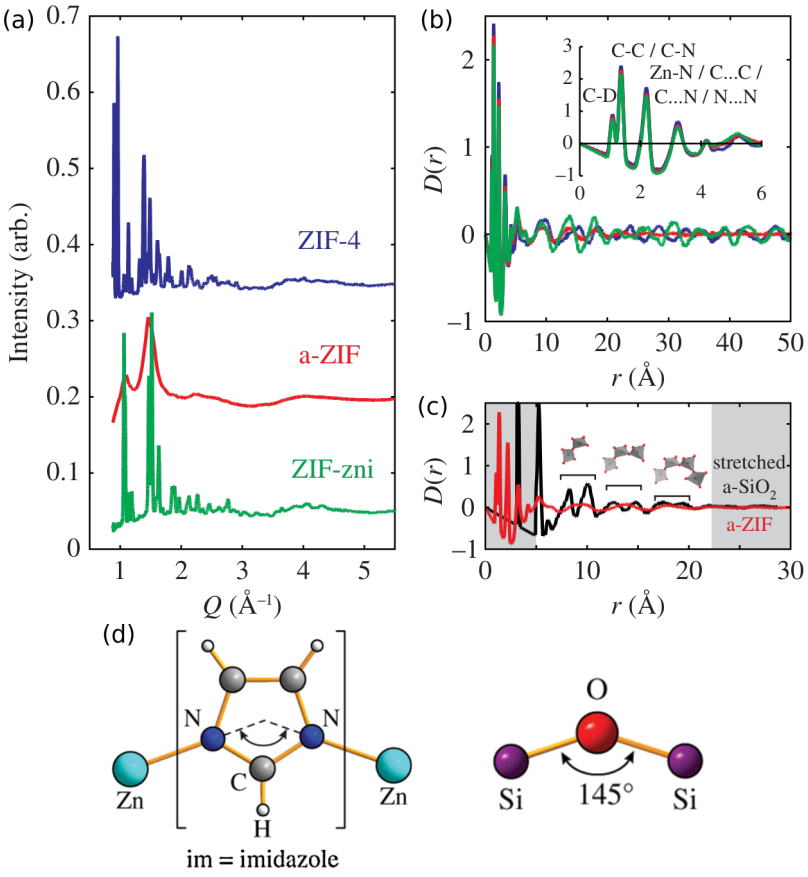

Figure 9: (a) Neutron total scattering $S(Q)$ at low Q for the desolvated ZIF-4 framework at 300 °C (top), amorphized a-ZIF product at 320 °C (middle), and recrystallized ZIF-zni at 400 °C (bottom). (b) The differential correlation functions $D(r)$, which are related to the $G(r)$, for the three phases. The inset highlights how the local structure of the three phases is practically identical. (c) Overlay of the $D(r)$ functions for a-ZIF and a-SiO_2, where the latter data set has been stretched in r such that the peaks that represent analogous Zn–Zn and Si–Si distances in the two materials overlap. (d) Representations of the Zn-im-Zn and Si-O-Si linkages in tetrahedral ZIF and silicate networks respectively. Reproduced from [98].

investigations into liquid MOFs [103, 104, 105]. On the other hand, the nucleation of ordered frameworks and intermediate species from solution has also been studied *in situ* [106, 107] (see Section 11 for more details on *in situ* studies on nucleation phenomena).

MOFs can also be susceptible to varying types of static disorder [109, 110]) and diverging stimulus-response effects occurring independent from the crystallographic symmetry. For example, octahedral M_6O_8 nodes with M = Zr and Hf have been observed to undergo distortions on heating by [111]. While no changes in the overall crystallographic nature of the framework could be observed from the Bragg reflections in Zr- and Hf-based analogues of MOFs NU-1000 and UiO-66, the distortions could be confirmed in real space, indicated by a splitting of the peak associated with the M-M pair distances. Similar distortions have been observed due to chemical interactions through adsorption or bridging of guest species [112]). This indicates that the node structures, like their linker counterparts, are not immune to external (or internal) stimuli and further suggests the ability to tune local electronic properties and possibly catalytic performance.

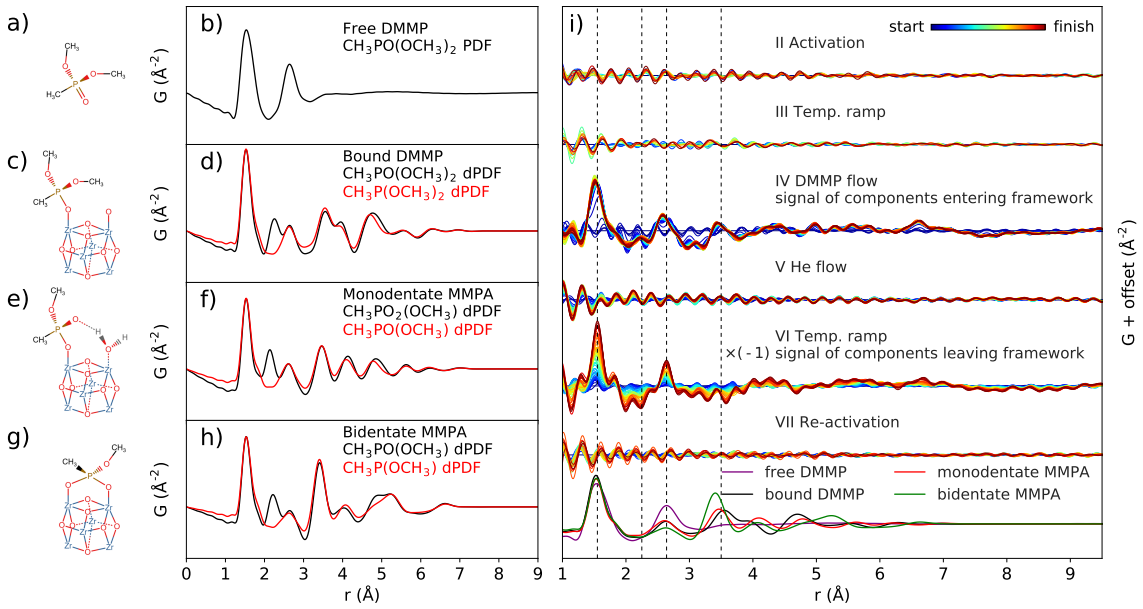

Figure 10: Schematic representations of the structures and corresponding simulated PDFs for an isolated DMMP molecule (a, b), bound DMMP (c, d), monodentate MMPA (e, f), and bidentate bound MMPA (g, h). Red curves show the difference PDFs (dPDFs) representing DMMP + DMMP-cluster pair distances with bridging oxygen considered as part of the cluster (black curves with bridging oxygen as part of DMMP). Models for simulated PDFs were obtained from DFT relaxation. (i) Experimental dPDFs for all the different steps of the process with the blue curve representing the start of a given step, and with each step offset for comparison. The simulated PDF for an isolated molecule of DMMP and the dPDFs of DMMP and MMPA binding states are plotted for reference at the bottom. Reproduced from [108].

Interactions with guest species are fundamental to the application of MOFs for gas storage and separations. In particular, various MOFs have been identified as potential catalysts for remediation and neutralization of toxic gas agents [113]). To optimize and implement these technologies requires efficient catalytic function and high cyclability, and therefore understanding of the reaction mechanism and associated structural effects on the framework. Rapid data collection and complex sample environments available at specialized synchrotron beamlines now allow for holistic investigations of the average and local structure under multivariable conditions. This has recently been used to study the uptake and neutralization of dimethyl methylphosphonate (DMMP) within the MOF UiO-67 [$Zr_6(\mu_3\text{-O})_4(\mu_3\text{-OH})_4(BPDC)_6$; BPDC: biphenyl-4,4 -dicarboxylate] [108] (Fig. 10). DMMP acts as a simulant for the nerve agent sarin, which can be taken up, bound, and detoxified by the framework. *In situ* total scattering experiments were performed with controlled temperature and gas-feed composition to study the guest and host structure during framework activation, loading, and re-activation. To test the mechanism of adsorption and neutralization, models for different mechanistic steps were prepared through periodic DFT relaxations of a crystallographic cell with one BPDC linker replaced by different binding interactions between DMMP or methyl methylphosphonate (MMPA) and the Zr_6 cluster. Possible signals could then be predicted through calculation of dPDFs associated with DMMP-DMMP or DMMP-cluster pairs, Fig. 10(a-h). Signals corresponding to adsorbed DMMP and its interaction with the framework could be extracted from experimental dPDF analysis, Fig. 10i). Distinct binding signals arise from P-Zr pair correlations during gas loading, and the distances agree well with bidentate bound MMPA, confirming the reaction mechanism.

8 Layered materials

Many materials form distinct layered motifs, which can succumb to a variety of two-dimensional defects in their formation. The effects of so-called *turbostratic* disorder, where the order between the orientations of separate layers is reduced or lost completely, was described by Warren [114]. Yet, this and other types of disorder involving random distributions of different preferred local interlayer interactions continue to plague crystal structure investigations today, and can be aided greatly by local structure information for materials as diverse as water ice [115], covalent–organic frameworks [116], and honeycomb structures formed by edge sharing $M^{n+}O_{6/2}^{(6n)}$ octahedra condensed into 6-fold rings [117, 118].

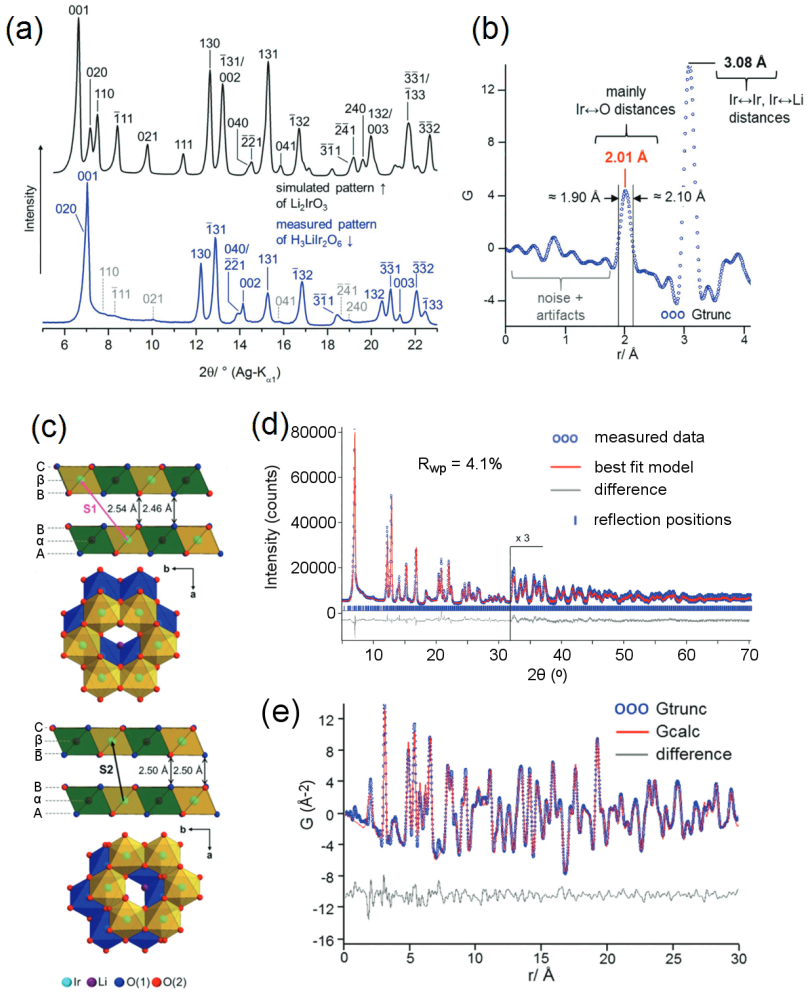

Figure 11: (a) Comparison of a simulated x-ray powder diffraction pattern from predicted structure (black) and experimental pattern of $H_3LiIr_2O_6$. (b) Excerpt of the measured PDF highlighting the constraints chosen for neighbor bond distances. (c) Examples of two different stacking patterns of two layers of the structure with stacking vectors used to describe the faulting scenarios. (d) The final Rietveld refinement obtained by unconstrained simulated annealing, which resulted in stacking vectors matching closely to that expected from structure considerations. (e) Measured PDF fitted using a 12-layer stacking supercell model obtained by global optimization. Reproduced from [117].

PDF analysis has been successful in determining the structure of many layered materials for which structure solution or refinement by reciprocal-space methods is not feasible. This has been shown for example in cases with very high stacking fault density, extensive disorder, and for layered nanomaterials. Examples and applications include CdSe quantum dots [45, 46] (see section 4 for details), vanadium oxide nanosheets for potassium-ion storage [119], carbon nitride [120] and cobalt-based [121] photocatalysts for hydrogen/oxygen evolution, and nanocrystalline zirconium phosphonate-phosphate structures as ion exchangers for nuclear fuel remediation [122]. Others include layered double hydroxide nanosheets [123], exfoliated-restacked metal dichalcogenides [124], and transition metal-carbide MXenes [125]. Improvements in refinement algorithms and posterior analysis of large models can be expected to aid in the modeling and interpretation of such systems [126].

PDF analysis was used to aid the detailed structure solution of the layered double oxide hydroxide $H_3LiIr_2O_6$. This material is attracting considerable attention as a potential pH sensor material and for its topological quantum spin liquid behaviour. The structure was solved by Bette *et al.* [117] through a tedious process involving a careful indexing of the observable peaks in the high-resolution diffraction patterns, assessment of possible stacking transitions from known structure analogues, calculation of diffraction patterns from those possible stacking patterns, and Rietveld refinement of the diffraction data with constrained models using a simulated annealing approach that helps to avoid local minima. Before the Rietveld analysis, PDF analysis was used to decide on the appropriate restraints of specific pair bond distances, and afterward, to check the agreement between the local structure and the expected stacking sequences, as depicted in Fig. 11.

9 Polycrystalline thin films

Historically, PDF was applied to bulk powders or bulk amorphous materials. In 2015 it was shown that signals could be extracted from thin films of polycrystalline or nanocrystalline films [127]. The signal from the film is very small compared to that of the substrate making these measurements challenging. However, the advent of high flux, high energy synchrotron sources, large area 2D detectors that are efficient even at these high energies [128], and more advanced data reduction algorithms [8] allow the extraction of very dilute signals [129]. This opened the door to extracting PDFs from thin films even in normal incidence, as shown in Figure 12.

Using this approach, it was possible to measure quantitatively reliable PDFs from polycrystalline and amorphous films of a few hundred nanometer thickness on substrates that were even millimeters thick [127]. The PDF extracted from a transparent conducting layer of indium tin oxide of 70 nm on a 4 mm glass slide substrate could even be successfully modeled [130]. Similarly, titania films synthesized under microwave electromagnetic radiation were shown to vary in amorphous and crystalline phase content, nanoparticle size, and film thickness as a function of synthesis temperature and microwave power [131]. This approach is obviously useful if your nano-sample happens to be in thin film geometry, but it also opens the door to doing spatially resolved measurements where films are heterogeneous. The ability to study thin films in this spatially resolved manner opens the door to lab-on-a-chip experiments, such as the case of dots of nanoparticles that can be written onto a substrate using an ink-jet printing device that writes using nanoparticle inks [132]. This is illustrated in Fig. 12(e) which shows a pixelation of one such chip. The dots containing nanoparticles are indicated in blue. However, in each of the pixels in the image we have a full and quantitative PDF that contains all the structural information about the nanoparticles that are deposited in that dot.

In cases where the signal from the film is very weak, it may be necessary to carry out a measurement in grazing incidence. This approach increases the signal from the film relative to the

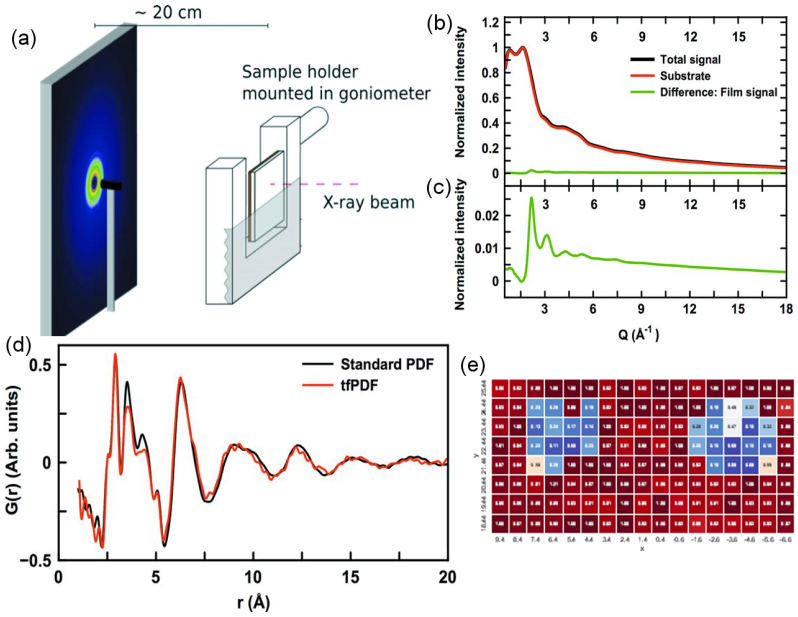

Figure 12: (a) Setup used for tfPDF measurements. The x-ray beam hits the substrate before the film. (b) Normalized data collected for sample 1A (black) and the clean substrate (red), and difference between the two (green), also shown on an expanded scale in (c). (d) Comparison between the tfPDF for sample 1A and a powder sample of similar composition, where the data were obtained for a sample measured in a standard capillary. (e) The distribution of nanoparticles on a chip extracted from tfPDFs. The pixels containing nanoparticles are indicated in blue. [127].

substrate, because the incident beam does not penetrate deeply into the substrate, whilst making a large footprint on the surface of the film [133]. This was used, for example, to show that thin Indium Gallium oxide films had distinct structures when compared to bulk material made using a gel method [134]. Grazing incidence thin film measurements are challenging experimentally, because the critical angle of high energy x-rays is very small for most films, and very stable and precise diffractometers are required, coupled with very stable x-ray optics. Such beamlines are becoming available, and it is expected that the importance of these grazing incidence thin film PDF measurements [133, 135, 136] will grow in the future.

A potential drawback for many thin film measurements is that the particles in the (polycrystalline) films take on a preferred crystallographic orientation (texture). For example, they may have more or less fiber texture with a preferred crystallographic direction lying perpendicular to the surface. This makes quantitative PDF analysis impossible unless steps are taken to mitigate this. Fortunately, approaches are emerging that will allow the PDF of textured samples to be studied [137].

10 Amorphous systems

The first applications of the PDF technique was for the structural study of amorphous materials and liquids for which reciprocal space diffraction techniques are inadequate. Still, the PDF was far from adequate, since only low-energy x-rays were available back then. The limited Q range reduces the real-space resolution and increases the effects of termination ripples in the Fourier transformation

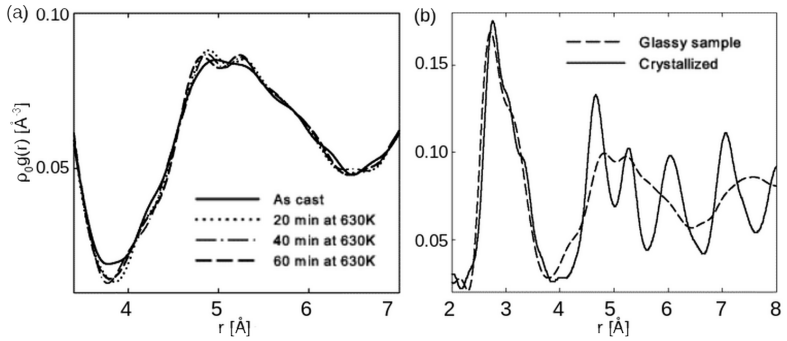

Figure 13: PDF of bulk metallic glass $Zr_{52.5}Cu_{17.9}Ni_{14.6}Al_{10.0}Ti_{5.0}$ (at.%) annealed under its glass transition temperature (630 K): (a) changes in PDF in the range of the second atomic shell after annealing for varying times. (b) Comparison between a sample annealed for 60 min and a crystallized sample (reproduced from [138]).

of the data, which can affect the the most precious signal at low r. This meant that the only quantities that could be reliably deduced were the average distance to the nearest neighbors and the coordination number (from the *radial distribution functions*, RDF)[139, 140]. With the modern development of high-energy radiation sources and 2D detectors, the complex structural details in the signal became accessible, uncovering the details of e.g. anisotropy and the formation of crystalline clusters. Modern PDF measurements can allow, for example, a more accurate representation of the shape of the first peak, medium-order structural interpretation using higher order peaks, and structural contributions from additional phases can be isolated using differential PDF methods ([1]).

The structure of amorphous systems may evolve over time, which is evidenced by observation of excess specific heat released by the breaking and reforming of bonds [142]. For example, x-ray PDF was used to explore the relaxation mechanism of metallic glasses during annealing at temperatures just below the glass transition temperature. Through a series of studies that started in the early 80's ([143] [144], and more recently and accurately 2007 ([138]), the structural relaxation mechanism of Zr-Cu-Ni-Al-Ti metallic glasses was probed with PDF. The PDF (see Fig. 13) showed that the evolution of the amorphous phase into the crystalline form involved the elimination of areas with both higher- and lower-than-average densities [138], rather than, the previously assumed, elimination of "free volume" (i.e., higher-than average pair distances) in the structure [142].

When the sample is heterogeneous, it is important to study the spatial (as well as temporal) changes across the sample. This is possible with x-rays, but also with electron diffraction carried out in an electron microscope. Electron beams can routinely be focused to resolutions of a few Å allowing for nanometer-scale mapping of local structure in glasses. Although electron-diffraction based PDF (ePDF) was introduced already in the 60's ([145]), it has only caught the eye of the community in the last decade due to recent improvements in the fabrication of very thin samples, microscopy hardware (e.g., lenses, detectors) and software-analysis tools [1], yielding sufficiently accurate PDFs that can be used for structural fitting [146]. The advent of faster data acquisition and analysis methods allows the ePDF measurements to be carried out in a spatially resolved way, resulting in a full PDF at each location in the thin sample with spatial resolutions at the nanoscale.

Recent studies used ePDF in a 4D-STEM mode scan to create local-structure maps that classified differences in local-structure in metallic glasses [147, 148] and organic polymer composite materials [149]. A more recent study by Rakita *et al.* [141] showed a generic concept for mapping structural heterogeneity in complex material systems, using structural features from ePDF in the

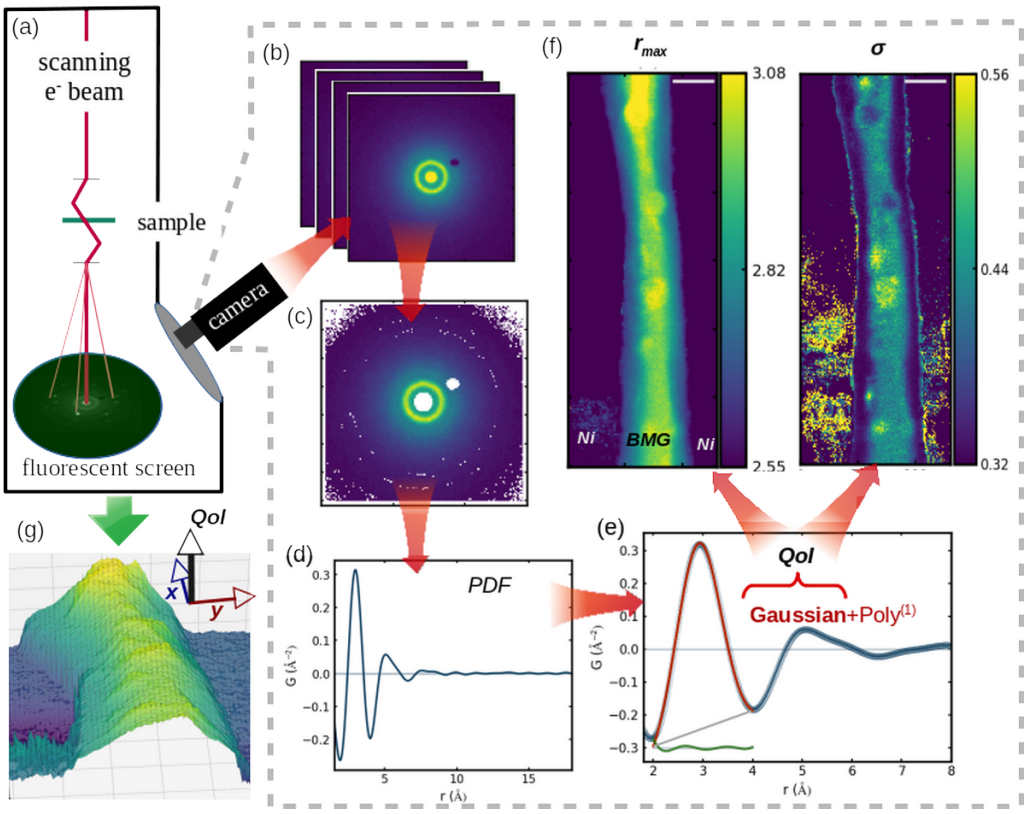

Figure 14: An overview summary of SNEM experimental data collection, data reduction, extraction of a quantity of interest (QoI), and visualization. (a) Schema of the electron-microscopy and the recording of diffraction patterns: patterns were collected using an external fast camera that recorded the diffraction data on a fluorescent screen detector. (b) An example of a recorded diffraction pattern gained from the amorphous part of the BMG. (c) Extraction of the virtual dark field using combined manual annular manual mask for the direct beam and an auto-masked damaged pixels (dark spot in b). (d) Derived PDF from the diffraction pattern. (e) Example of an extraction of a QoI - here a Gaussian + first order polynomial, where blue curve is data, red is fit, and green is the difference between fit and data curved. (f) Maps of the QoI r_{max}, which is the maximum of the first peak, and σ, which is the peak width. The maps in (f) show structural heterogeneity in the BMG, where r_{max}, reflects the average pair-distances and σ reflects the distribution of the existing pairs within the first coordination shell. The scale bars in (f) maps refer to 100 nm. (g) a 3D representation of a QoI map that summarizes the concept behind SNEM; this specific example shows a 3D r_{max} QoI SNEM map shown in (f)).[141]

form of scalar quantities of interest (QoI). From a focused ion beam (FIB) lift-out of a hot-rolled amorphous $Zr_{65}Cu_{17.5}Ni_{10}Al_{7.5}$ bulk metallic glass (BMG) capped with a crystalline Ni composite, electron diffraction images were collected with a 3 nm spatial resolution and reduced to 1-D PDF's. The reduced 1-D PDF plots, were then used to extract local-order structural quantities of interest (QoI), such as the average inter-atomic pair distance using the first PDF peak-maximum position, and the atomic-number weighted distribution of inter-atomic bond lengths at the first coordination by extracting the PDF peak width. Recording the value of each QoI as a function of position resulted in a structure-oriented microscopy, and with a positional resolution of just a few nm, scanning nano-structure electron microscopy (SNEM) maps, as shown in Fig. 14, could be generated. After the BMG was distinguished from the surrounding Ni, the 2D QoI-based SNEM maps (panel

f) reflect, with ~ 5 nm spatial accuracy, variations in local-order, composition, and local-structure. The r_max map, which represents the average pair-distance, yields information about the Zr contribution, as also evident from an EELS map from the same region [141]. From the map of the width, σ, of the first PDF peak, sharper and narrower peaks were observed coincident with Zr-rich areas (brighter yellow in r_max map), suggesting variations in the number of different chemical species in the two regions. However, the PDF contains more than just chemical information, allowing in principle differentiation between random solid solution, segregated, relaxed, or intermatallic regions [150]). These examples emphasize the potential of PDF for investigating the spatial or temporal heterogeneity of the local structure in materials at a nanometer length scale.

11 Nucleation of crystallites

Crystal growth can happen via self-assembly of smaller units referred to as crystallization centers, such as monomers, molecular clusters, or nanocrystals [151]. The crystallization centers can appear spontaneously in a medium (primary nucleation) - often in a super-saturated medium at a given temperature or pressure [152], for instance when ice crystals nucleate in water below the freezing temperature. They can also be introduced intentionally or accidentally to a system (secondary nucleation). The key goal of any synthesis is to have control of the morphology, composition, and structure of the product. Controlling nucleation can guide the consequently grown phase, and therefore the nucleation processes are not only interesting in and of themselves. They are widely utilized in controlling the synthesis of new and better materials, for a wide range of applications where functional materials are used, e.g. batteries, fuel cells, solar cells, electronics, sensors, catalysts, and for medical imaging. Examples of synthesis processes that utilize nucleation are sol-gel, molten-salt, precipitation, and solvo-/hydrothermal synthesis.

Nuclei are clustered species in a bulk medium that posses a unique structural order that is different from the surrounding bulk. These clusters do not span over long distances, which infers that understanding nucleation requires a probe that can follow the evolution at the short- to mid- to long-range order. Knowing already that PDF is a probe for local order, it has been widely used for tracing and reconstructing the structures of nuclei. PDF has been used to study nucleation during the sol-gel synthesis of SiO_2-TiO_2 aerogels [154], during the reduction-precipitation synthesis of Pt nanoparticles [155] and during the molten-salt synthesis of MgO in $NaNO_3$ [156]. But the vast majority of scattering measurements on nucleation processes have examined the particularly promising process of hydrothermal or solvothermal synthesis. The development of *in situ* setups has enabled studies of solvo-/hydrothermal synthesis, a very widely used method to synthesize materials at both elevated pressures and temperatures inside thick-walled closed containers. The *in situ* setups bypassed the use of a container, whose walls cannot be penetrated by x-rays, by using capillaries with pressure supplied at each end. PDF has been used to determine the evolution of the structure from precursor to product for a wide range of materials, including SnO_2 [157] and CeO_2 [158] nanoparticles, yttria-stabilized zirconia [159], Li-Fe-Mn-phosphate cathode materials [160, 161], nanoparticles of maghemite [162], WO_3 [163, 153], $ZnWO_4$ [164] and MnO_2 [165], lepidocrocite-type layered titanates [166], Pd-Pt core-shell nanoparticles [167], ZIF-8 [106] and UiO-66 metal-organic framework materials [107], zeolites [168], hierarchical and microporous aluminophosphate [169], Sr-Ba niobates [170] and $ZnAl_2O_4$ nanocrystals [171].

In the study by Juelsholt *et al.* [153], for example, the mechanisms for the formation of tungsten oxide nanoparticles from the initial precursor to the final crystalline particles were elucidated. Monitoring the nucleation process both in water and in the solvent oleylamine, the authors could deconstruct the nucleation mechanisms of the WO_3 particles. Despite the formation of the same Keggin-cluster in both precursor solutions, and its similarity to the end product, they found that

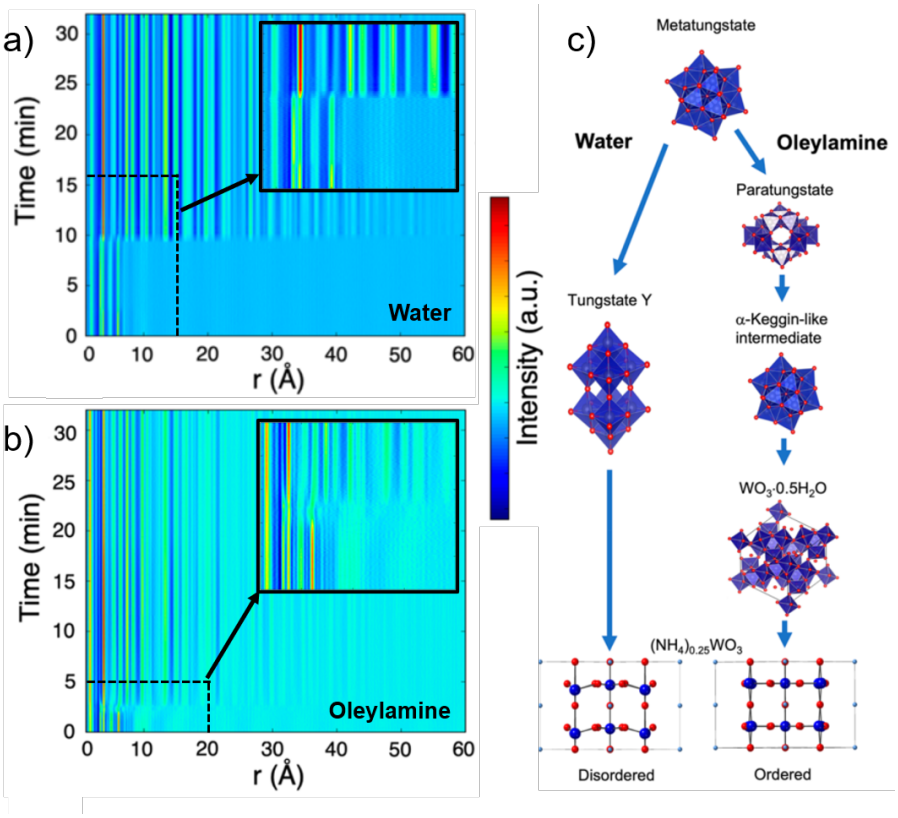

Figure 15: Time-resolved PDFs obtained during the synthesis of the hexagonal tungsten bronze$(NH_4)_{0.25}WO_3$ nanoparticles in water (a) and in oleylamine (b). The insets show the region just before crystallization. c) The suggested formation pathway of nucleation in water and oleylamine, based on the time-resolved PDFs. In both solutions, the process starts with the initial dissolution of the crystalline metatungstate precursor. In water, the pathway goes via the formation of α-Keggin-structured clusters, which upon heating enter an equilibrium with a Tungstate Y cluster $W_{10}O_{32}$, from which the tungsten bronze crystallize into 70 nm nanoparticles with a disordered WO_3 structure. In oleylamine, the metatungstate also dissolves to form α-Keggin-structured clusters, which then quickly transform into an amorphous phase similar to the paratungstate cluster. Then, moments before crystallization, the amorphous phase breaks up and another α-Keggin-like structure is observed. Crystallization happens in two steps; first nanoparticles with a cubic pyrochlore structure $WO_3 \cdot 0.5H_2O$ form, secondly they undergo a phase change into the hexagonal tungsten oxide bronze structure, as seen in the synthesis in water, however with no clear structural disorder on the tungsten sites. Reproduced from [153].

the reaction route in water went through less steps leading to a disordered WO_3 structure, while the oleylamine route went through more steps but gave a well ordered WO_3 structure. More details about the results can be found in Chapter X [note to editor: crossref to chapter on "In situ scattering studies of material formation in wet-chemical synthesis" by Kirsten Jensen].

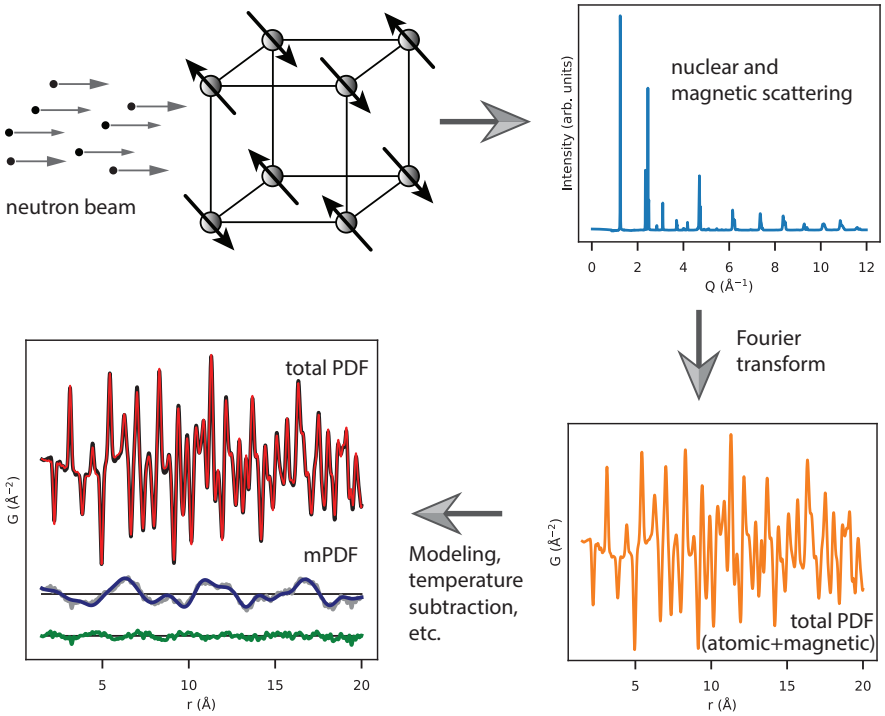

Figure 16: Schematic illustration of how the mPDF can be obtained for a typical neutron PDF experiment. After fitting a structural model to the PDF, which contains both the structural and magnetic signal, the magnetic part of the signal cannot be adequately fitted and will be left in the difference curve.

12 Magnetic crystals

PDF can also be applied to studies of magnetic structure using magnetic PDF (mPDF) analysis [172, 173]. Just like the atomic PDF, the mPDF provides a real-space map of pairwise correlations between magnetic moments, although it is more complex than the atomic PDF because it involves orientational correlations (e.g. ferromagnetic versus antiferromagnetic alignment) as well as spatial correlations between moments. mPDF analysis must be done using neutrons, which scatter from magnetic moments relatively strongly, whereas the magnetic scattering cross section for x-rays is too small to make mPDF analysis possible with current methodologies. Here, we briefly introduce mPDF analysis of neutron data and provide an example of its application to the antiferromagnetic oxide $NaMnO_2$.

The most common way to obtain the mPDF is to measure it simultaneously with the atomic PDF in a standard neutron PDF experiment on a magnetic material. The total PDF pattern obtained from the usual data reduction protocols is the sum of the atomic PDF and the mPDF. The mPDF is typically isolated either by (1) modeling the atomic PDF and subtracting it from the total PDF signal; or (2) collecting a PDF pattern at a temperature where the magnetic correlations are negligible and subtracting it from the PDF patterns with non-negligible magnetic contributions. The general approach to obtaining the mPDF is outlined schematically in Fig. 16. Whether the magnetic structure is of primary interest or merely a curiosity (or annoyance!) in the data, the

ability to recognize and model the mPDF is valuable for performing a complete and reliable PDF analysis of any system of interest.

The inorganic material α-$NaMnO_2$ provides a useful example of combined atomic and magnetic PDF analysis [174]. This compound is the end member for the Na_xMnO_2 system, which has been investigated as a potential battery electrode material. $NaMnO_2$ is also magnetic, with the spins on the Mn^{3+} ions exhibiting long-range antiferromagnetic order below $T_N = 45$ K, and short-range antiferromagnetic correlations persisting to significantly higher temperatures. The interesting aspect of this material from a magnetic point of view is that the Mn^{3+} spins form networks of isosceles triangles in the crystallographic structure, making $NaMnO_2$ a geometrically frustrated antiferromagnet. As illustrated in Fig. 17(c), one side of the triangle (r_1) is shorter than the other two, so the strong antiferromagnetic interactions lead to oppositely aligned spins on either end of r_1. However, the two isosceles legs (r_2 and r_3) are equal in length. Consequently, whether the spin on

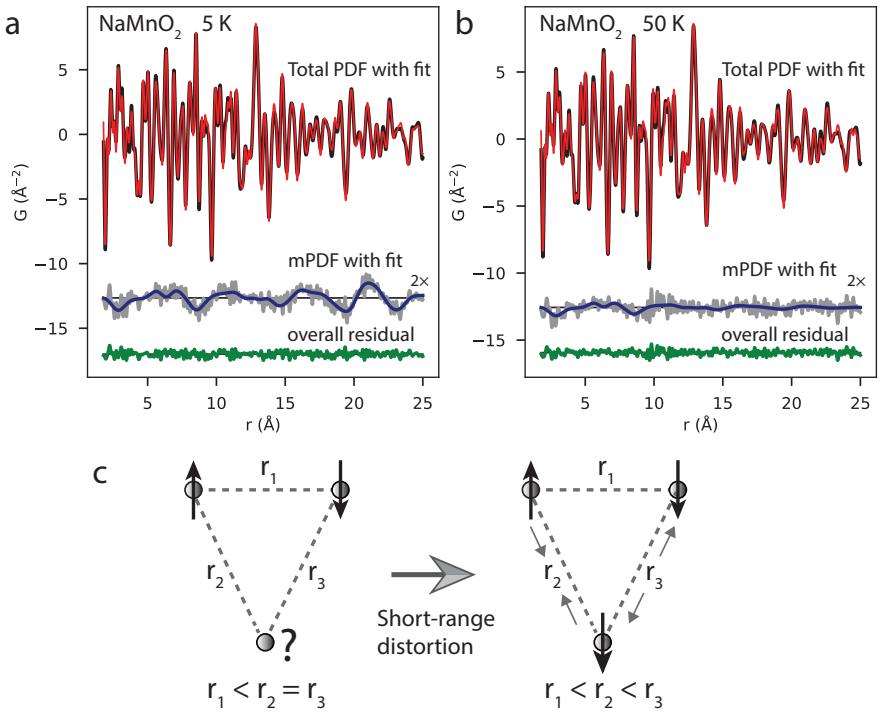

Figure 17: Joint atomic and magnetic PDF analysis of $NaMnO_2$ at 5 K (a) and 50 K (b). Black and red curves are the total PDF data and the total PDF fit, respectively. The mPDF data (gray curves) reveal long-range antiferromagnetic correlations at 5 K and short-range correlations at 50 K, and they are well described by the fits (blue curves). (c) Triangular motif of Mn^{3+} spins in $NaMnO_2$. The triangles are isosceles in the average structure (left), resulting in magnetic frustration. The PDF analysis shows that a short-range structural distortion lifts this degeneracy locally, relieving the magnetic frustration and allowing a unique magnetic ground state to be selected.

the lower vertex is up or down, the spin alignment along one leg will be antiferromagnetic (favored) while the other will be ferromagnetic (disfavored), thus frustrating the system. How the system selects a unique, long-range ordered magnetic ground state below 45 K despite the degeneracy between the two isosceles legs remained a mystery for a long time.

This mystery was resolved through a combined atomic and magnetic PDF analysis of $NaMnO_2$,

which revealed that a short-range structural distortion breaks the isosceles symmetry locally and promotes short-range antiferromagnetic correlations along the shorter isosceles leg [see Fig. 17(c)]. The magnetic correlations grow in magnitude and spatial extent as the temperature is lowered and eventually transition to genuine long-range magnetic order, even while the structural distortion exists only on short length scales. Representative PDF patterns collected at 5 K (with long-range magnetic order) and 50 K (with short-range magnetic order) are shown in Fig. 17(a, b). The black curve is the experimental total PDF, with the best-fit total PDF overlaid as the red curve. The gray and blue curves (offset vertically and multiplied by two for clarity) represent the mPDF data and fit, respectively. The small overall fit residual (lower green curve) indicates a good fit to the total PDF. At 50 K, the mPDF pattern is strongly damped at high r, indicating a finite magnetic correlation length, and the overall magnitude is smaller due to increased thermal fluctuations of the magnetization.

By tracking the behavior of the local structural distortion and the magnetic correlations as a function of temperature across the magnetic transition, this work established a novel coupling between magnetism and a short-range structural distortion to relieve the magnetic frustration. More generally, this example highlights the power of combined atomic and magnetic PDF analysis in magnetic materials. Such an approach will be valuable for numerous other systems with coupling between the magnetic and structural properties.

13 Future development

Here, we point out some promising directions in PDF analysis that address emerging challenges in materials science.

One reason why the conventional powder diffraction and PDF techniques have become popular in the scientific community is that reliable, trustworthy, and easy-to-use data analysis and modeling programs have become available. For example, in the PDF context, GUI (graphical user interface) programs such as xPDFsuite [175] and PDFgui [14], have been very popular [2]. In the future, especially in view of "big-data" and cloud-computing, we would expect more web-based PDF analysis platforms, such as 'PDF in the cloud' (PDFitc) [63], to help users analyze and interpret their PDF data in a more convenient manner, and to build knowledge of materials. In principle, these platforms can become single-button analyzers for PDF making materials characterization more straightforward by sharing community expertise.

In the wake of the implementation of new data tools such as materials databases, machine learning, and high-throughput methods, [176] new approaches to PDF analysis have recently been created, such as automated structure-mining based conventional modeling approaches [76, 60] and machine learning to suggest the space group of novel nanomaterials [177].

Most PDF work is performed using synchrotron x-rays or spallation neutrons, with only some using electrons. Better utilization of these precious resources is made possible by greater automation of experiments, with the community further pushing in the direction of *autonomation*, meaning that an *in situ* experiment is evolving in time with input parameters being determined by a mathematical decision algorithm based on results from previous measurements. This is particularly important when we seek to explore an input parameter space that is high dimensional (many control parameters) in a smart way [178, 179]. At the time of writing these efforts are yet to be demonstrated for PDF, but with improvements in infrastructure for automation and automated data reduction in a streaming context [180, 181, 182], this is just around the corner.

With the growth of *in situ* PDF experimentation [183, 184, 185, 108], the coupling of computed

tomography with PDF [186, 187] and spatial resolution that can get down to 10-100 um with x-rays [187, 186] and 10-100 nm with electrons [147, 148, 149], advances in reaction evolution and phase transition evolution studies with high spatial resolution will start to have significant impacts in our understanding of material processing. Integration with automation can unlock the capability to trace boundaries in structural evolution at the nanoscale, especially at early stages where long-range order is absent. Also, introducing floating liquid phase cells in a TEM [188] and integrating it with electron-PDF analysis can unlock the possibility to investigate nucleation reactions at the nanoscale.

14 Acknowledgements

S.H.S, Y.S.R., L.Y. and S.T. were supported by the U.S. National Science Foundation through grant DMREF-1922234. S.J.L.B was supported by the U.S. Department of Energy, Office of Science, Office of Basic Energy Sciences (DOE-BES) under contract No. DE-SC0012704. M.W.T. gratefully acknowledges support from BASF. Soham Banerjee and Robert Koch are acknowledged for valuable discussions.

References

[1] T. Egami and S. J. L. Billinge. *Underneath the Bragg peaks: structural analysis of complex materials*. Elsevier, Amsterdam, 2nd edition, 2012.

[2] Simon J. L. Billinge. The rise of the X-ray atomic pair distribution function method: a series of fortunate events. *Philosophical Transactions of the Royal Society A: Mathematical, Physical and Engineering Sciences*, 377(2147):20180413, June 2019.

[3] Mois I. Aroyo. *International Tables for Crystallography*, volume A, Space-group Symmetry. Wiley, 6th edition, 2017.

[4] Simon J L Billinge, Soham Banerjee, Emil S Bozin, Kirsten M Ø Jensen, Benjamin A Frandsen, Maxwell W Terban, and Robert J Koch. *PDF to the people: an atomic pair distribution function analysis primer*. unpublished, 2021.

[5] P. F. Peterson, D. Olds, M. T. McDonnell, and K. Page. Illustrated formalisms for total scattering data: a guide for new practitioners. *Journal of Applied Crystallography*, 54(1):317–332, February 2021. Number: 1 Publisher: International Union of Crystallography.

[6] D. Olds, C. N. Saunders, M. Peters, T. Proffen, J. Neuefeind, and K. Page. Precise implications for real-space pair distribution function modeling of effects intrinsic to modern time-of-flight neutron diffractometers. *Acta Crystallographica Section A: Foundations and Advances*, 74(4):293–307, July 2018.

[7] P. Debye. Dispersion of Röntgen rays. *Annalen der Physik (Berlin, Germany)*, 351:809–823, 1915.

[8] P. Juhás, T. Davis, C. L. Farrow, and S. J. L. Billinge. PDFgetX3: a rapid and highly automatable program for processing powder diffraction data into total scattering pair distribution functions. *Journal of Applied Crystallography*, 46(2):560–566, April 2013.

[9] P.f. Peterson, M. Gutmann, Th. Proffen, and S.j.l. Billinge. PDFgetN: a user-friendly program to extract the total scattering structure factor and the pair distribution function from neutron powder diffraction data. *Journal of Applied Crystallography*, 33(4):1192, August 2000. Publisher: Wiley-Blackwell.

[10] P. Juhás, J. N. Louwen, L. van Eijck, E. T. C. Vogt, and S. J. L. Billinge. PDFgetN3: atomic pair distribution functions from neutron powder diffraction data using ad hoc corrections. *Journal of Applied Crystallography*, 51(5):1492–1497, October 2018. Publisher: International Union of Crystallography.

[11] B. H. Toby and R. B. Von Dreele. GSAS-II: the genesis of a modern open-source all purpose crystallography software package. *Journal of Applied Crystallography*, 46(2):544–549, April 2013. Publisher: International Union of Crystallography.

[12] A. A. Coelho. TOPAS Academic: General Profile and Structure Analysis Software for Powder Diffraction Data; Bruker AXS, 2004.

[13] A. Soper. GudrunN and GudrunX : programs for correcting raw neutron and X-ray diffraction data to differential scattering cross section. *undefined*, 2011.

[14] C. L. Farrow, P. Juhás, J. W. Liu, D. Bryndin, E. S. Bozin, J. Bloch, Th Proffen, and S. J. L. Billinge. PDFfit2 and PDFgui: computer programs for studying nanostructure in crystals. *Journal of Physics: Condensed Matter*, 19(33):335219, July 2007.

[15] G. H. Kwei, A. C. Lawson, S. J. L. Billinge, and S. W. Cheong. Structures of the ferroelectric phases of barium titanate. *The Journal of Physical Chemistry*, 97(10):2368–2377, March 1993.

[16] George H. Kwei, Simon J. L. Billinge, S.-W. Cheong, and Jay G. Saxton. Pair-distribution functions of ferroelectric perovskites: Direct observation of structural ground states. *Ferroelectrics*, 164(1):57–73, February 1995.

[17] M.S. Senn, D.A. Keen, T.C.A. Lucas, J.A. Hriljac, and A.L. Goodwin. Emergence of Long-Range Order in $BaTiO_3$ from Local Symmetry-Breaking Distortions. *Physical Review Letters*, 116(20):207602, May 2016.

[18] V. Westphal, W. Kleemann, and M. D. Glinchuk. Diffuse phase transitions and random-field-induced domain states of the "relaxor" ferroelectric $PbMg_{1/3}Nb_{2/3}O_3$. *Physical Review Letters*, 68(6):847–850, February 1992.

[19] I.-K. Jeong, T. W. Darling, J. K. Lee, Th. Proffen, R. H. Heffner, J. S. Park, K. S. Hong, W. Dmowski, and T. Egami. Direct Observation of the Formation of Polar Nanoregions in $Pb(Mg_{1/3}Nb_{2/3})O_3$ Using Neutron Pair Distribution Function Analysis. *Physical Review Letters*, 94(14):147602, April 2005.

[20] I.-K. Jeong and J. K. Lee. Local structure and medium-range ordering in relaxor ferroelectric $Pb(Zn_{1/3}Nb_{2/3})O_3$ studied using neutron pair distribution function analysis. *Applied Physics Letters*, 88(26):262905, June 2006.

[21] I.-K. Jeong, J. K. Lee, and R. H. Heffner. Local structural view on the polarization rotation in relaxor ferroelectric (1-x)$Pb(Zn_{1/3}Nb_{2/3})O_3$ – x$PbTiO_3$. *Applied Physics Letters*, 92(17):172911, April 2008.

[22] Andrew L. Goodwin, Simon A. T. Redfern, Martin T. Dove, David A. Keen, and Matthew G. Tucker. Ferroelectric nanoscale domains and the 905 K phase transition in $SrSnO_3$: A neutron total-scattering study. *Physical Review B*, 76(17):174114, November 2007.

[23] Marc Widenmeyer, Stefano Checchia, Xingxing Xiao, Marco Scavini, and Anke Weidenkaff. Effects of Nanodomains on Local and Long-Range Phase Transitions in Perovskite-Type $Eu_{0.8}Ca_{0.2}TiO_{3-\delta}$. *Nanomaterials*, 10(4), April 2020.

[24] S. J. L. Billinge, R. G. DiFrancesco, G. H. Kwei, J. J. Neumeier, and J. D. Thompson. Direct Observation of Lattice Polaron Formation in the Local Structure of $La_{1-x}Ca_xMnO_3$. *Physical Review Letters*, 77(4):715–718, July 1996.

[25] Bing Li, Despina Louca, Shinichiro Yano, Luke G. Marshall, Jianshi Zhou, and John B. Goodenough. Insulating Pockets in Metallic $LaNiO_3$. *Advanced Electronic Materials*, 2(2):1500261, 2016.

[26] Long Yang, Robert J. Koch, Hong Zheng, J. F. Mitchell, Weiguo Yin, Matthew G. Tucker, Simon J. L. Billinge, and Emil S. Bozin. Two-orbital degeneracy lifted local precursor to a metal-insulator transition in $MgTi_2O_4$. *Physical Review B*, 102(23):235128, December 2020.

[27] E. S. Bozin, T. Chatterji, and S. J. L. Billinge. Local structure of ReO_3 at ambient pressure from neutron total-scattering study. *Physical Review B*, 86(9):094110, September 2012.

[28] Emil S. Bozin, Ruidan Zhong, Kevin R. Knox, Genda Gu, John P. Hill, John M. Tranquada, and Simon J. L. Billinge. Reconciliation of local and long-range tilt correlations in underdoped $La_{2-x}Ba_xCuO_4$ ($0 \leq x \leq 0.155$). *Physical Review B*, 91(5):054521, February 2015.

[29] Peter J. Chupas, Santanu Chaudhuri, Jonathan C. Hanson, Xiangyun Qiu, Peter L. Lee, Sarvjit D. Shastri, Simon J. L. Billinge, and Clare P. Grey. Probing Local and Long-Range Structure Simultaneously: An *In Situ* Study of the High-Temperature Phase Transition of α-AlF_3. *Journal of the American Chemical Society*, 126(15):4756–4757, April 2004.

[30] Alexander N. Beecher, Octavi E. Semonin, Jonathan M. Skelton, Jarvist M. Frost, Maxwell W. Terban, Haowei Zhai, Ahmet Alatas, Jonathan S. Owen, Aron Walsh, and Simon J. L. Billinge. Direct Observation of Dynamic Symmetry Breaking above Room Temperature in Methylammonium Lead Iodide Perovskite. *ACS Energy Letters*, 1(4):880–887, October 2016.

[31] P. Tong, Despina Louca, Nara Lee, and S.-W. Cheong. Oxygen displacements and magnetoelectric coupling in $LuMnO_3$. *Physical Review B*, 86(9):094419, September 2012.

[32] Alexandra S. Gibbs, Kevin S. Knight, and Philip Lightfoot. High-temperature phase transitions of hexagonal $YMnO_3$. *Physical Review B*, 83(9):094111, March 2011.

[33] Sandra H. Skjærvø, Quintin N. Meier, Mikhail Feygenson, Nicola A. Spaldin, Simon J.L. Billinge, Emil S. Bozin, and Sverre M. Selbach. Unconventional Continuous Structural Disorder at the Order-Disorder Phase Transition in the Hexagonal Manganites. *Physical Review X*, 9(3):031001, July 2019.

[34] G Nénert, M Pollet, S Marinel, G R Blake, A Meetsma, and T T M Palstra. Experimental evidence for an intermediate phase in the multiferroic $YMnO_3$. *Journal of Physics: Condensed Matter*, 19(46):466212, November 2007.

[35] Megan M. Butala, Martin Mayo, Vicky V. T. Doan-Nguyen, Margaret A. Lumley, Claudia Göbel, Kamila M. Wiaderek, Olaf J. Borkiewicz, Karena W. Chapman, Peter J. Chupas, Mahalingam Balasubramanian, Geneva Laurita, Sylvia Britto, Andrew J. Morris, Clare P. Grey, and Ram Seshadri. Local Structure Evolution and Modes of Charge Storage in Secondary Li-FeS_2 Cells. *Chemistry of Materials*, 29(7):3070–3082, April 2017.

[36] Yang Ren and Xiaobing Zuo. Synchrotron X-Ray and Neutron Diffraction, Total Scattering, and Small-Angle Scattering Techniques for Rechargeable Battery Research. *Small Methods*, 2(8):1800064, 2018.

[37] Baris Key, Mathieu Morcrette, Jean-Marie Tarascon, and Clare P. Grey. Pair Distribution Function Analysis and Solid State NMR Studies of Silicon Electrodes for Lithium Ion Batteries: Understanding the (De)lithiation Mechanisms. *Journal of the American Chemical Society*, 133(3):503–512, January 2011.

[38] Kamila M. Wiaderek, Olaf J. Borkiewicz, Nathalie Pereira, Jan Ilavsky, Glenn G. Amatucci, Peter J. Chupas, and Karena W. Chapman. Mesoscale Effects in Electrochemical Conversion: Coupling of Chemistry to Atomic- and Nanoscale Structure in Iron-Based Electrodes. *Journal of the American Chemical Society*, 136(17):6211–6214, April 2014.

[39] Damien Dambournet, Karena W. Chapman, Mathieu Duttine, Olaf Borkiewicz, Peter J. Chupas, and Henri Groult. Lithium Insertion Mechanism in Iron-Based Oxyfluorides with Anionic Vacancies Probed by PDF Analysis. *ChemistryOpen*, 4(4):443–447, August 2015.

[40] Jonas Sottmann, Marco Di Michiel, Helmer Fjellvåg, Lorenzo Malavasi, Serena Margadonna, Ponniah Vajeeston, Gavin B. M. Vaughan, and David S. Wragg. Chemical Structures of Specific Sodium Ion Battery Components Determined by *Operando* Pair Distribution Function and X-ray Diffraction Computed Tomography. *Angewandte Chemie International Edition*, 56(38):11385–11389, 2017.

[41] Valeri Petkov, Binay Prasai, Shiyao Shan, Yang Ren, Jinfang Wu, Hannah Cronk, Jin Luo, and Chuan-Jian Zhong. Structural dynamics and activity of nanocatalysts inside fuel cells by *in operando* atomic pair distribution studies. *Nanoscale*, 8(20):10749–10767, May 2016.

[42] Matthew J. Krogstad, Stephan Rosenkranz, Justin M. Wozniak, Guy Jennings, Jacob P. C. Ruff, John T. Vaughey, and Raymond Osborn. Reciprocal space imaging of ionic correlations in intercalation compounds. *Nature Materials*, 19(1):63–68, January 2020.

[43] C. B. Murray, D. J. Norris, and M. G. Bawendi. Synthesis and characterization of nearly monodisperse CdE (E = sulfur, selenium, tellurium) semiconductor nanocrystallites. *Journal of the American Chemical Society*, 115(19):8706–8715, September 1993.

[44] A. P. Alivisatos. Semiconductor Clusters, Nanocrystals, and Quantum Dots. *Science*, 271(5251):933–937, February 1996.

[45] A. S. Masadeh, E. S. Bozin, C. L. Farrow, G. Paglia, P. Juhás, A. Karkamkar, M. G. Kanatzidis, and S. J. L. Billinge. Quantitative size-dependent structure and strain determination of CdSe nanoparticles using atomic pair distribution function analysis. *Phys. Rev. B*, 76:115413, 2007.

[46] Xiaohao Yang, Ahmad S. Masadeh, James R. McBride, Emil S. Bozin, Sandra J. Rosenthal, and Simon J. L. Billinge. Confirmation of disordered structure of ultrasmall CdSe nanoparticles from x-ray atomic pair distribution function analysis. *Physical Chemistry Chemical Physics*, 15(22):8480–8486, 2013.

[47] Reinhard B. Neder and Vladimir I. Korsunskiy. Structure of nanoparticles from powder diffraction data using the pair distribution function. *Journal of Physics: Condensed Matter*, 17(5):S125–S134, January 2005. Publisher: IOP Publishing.

[48] Troels Lindahl Christiansen, Susan R. Cooper, and Kirsten M. Ø. Jensen. There's no place like real-space: elucidating size-dependent atomic structure of nanomaterials using pair distribution function analysis. *Nanoscale Advances*, 2(6):2234–2254, June 2020. Publisher: RSC.

[49] Jonathan Owen and Louis Brus. Chemical Synthesis and Luminescence Applications of Colloidal Semiconductor Quantum Dots. *Journal of the American Chemical Society*, 139(32):10939–10943, August 2017. Publisher: American Chemical Society.

[50] Sarah M. Harrell, James R. McBride, and Sandra J. Rosenthal. Synthesis of Ultrasmall and Magic-Sized CdSe Nanocrystals. *Chemistry of Materials*, 25(8):1199–1210, April 2013. Publisher: American Chemical Society.

[51] P. Juhás, C. Farrow, X. Yang, K. Knox, and S. Billinge. Complex modeling: a strategy and software program for combining multiple information sources to solve ill posed structure and nanostructure inverse problems. *Acta Crystallographica Section A: Foundations and Advances*, 71(6):562–568, November 2015.

[52] T. Proffen and R. B. Neder. DISCUS: a program for diffuse scattering and defect-structure simulation. *Journal of Applied Crystallography*, 30(2):171–175, April 1997.

[53] K. Page, T. C. Hood, Th Proffen, and R. B. Neder. Building and refining complete nanoparticle structures with total scattering data. *Journal of Applied Crystallography*, 44(2):327–336, April 2011.

[54] Agnieszka Poulain, Izabela Sobczak, and Maria Ziolek. Size of Au-Nanoparticles Supported on Mesostructural Cellular Foams Studied by the Pair Distribution Function Technique. *Crystal Growth & Design*, 16(10):5985–5993, October 2016.

[55] Jinfang Wu, Shiyao Shan, Valeri Petkov, Binay Prasai, Hannah Cronk, Pharrah Joseph, Jin Luo, and Chuan-Jian Zhong. Composition–Structure–Activity Relationships for Palladium-Alloyed Nanocatalysts in Oxygen Reduction Reaction: An *Ex-Situ*/*In-Situ* High Energy X-ray Diffraction Study. *ACS Catalysis*, 5(9):5317–5327, September 2015.

[56] Blaise Fleury, Robinson Cortes-Huerto, Olivier Taché, Fabienne Testard, Nicolas Menguy, and Olivier Spalla. Gold Nanoparticle Internal Structure and Symmetry Probed by Unified Small-Angle X-ray Scattering and X-ray Diffraction Coupled with Molecular Dynamics Analysis. *Nano Letters*, 15(9):6088–6094, September 2015.

[57] Chanaka Kumara, Xiaobing Zuo, Jan Ilavsky, Karena W. Chapman, David A. Cullen, and Amala Dass. Super-Stable, Highly Monodisperse Plasmonic Faradaurate-500 Nanocrystals with 500 Gold Atoms: Au 500(SR) 120. *Journal of the American Chemical Society*, 136(20):7410–7417, May 2014.

[58] Katharine Page, Thomas Proffen, Humberto Terrones, Mauricio Terrones, Lily Lee, Yan Yang, Susanne Stemmer, Ram Seshadri, and Anthony K Cheetham. Direct observation of the structure of gold nanoparticles by total scattering powder neutron diffraction. *Chemical Physics Letters*, 393(4):385–388, August 2004.

[59] V. Petkov and S. D. Shastri. Element-specific structure of materials with intrinsic disorder by high-energy resonant x-ray diffraction and differential atomic pair-distribution functions: A study of PtPd nanosized catalysts. *Physical Review B*, 81(16):165428, April 2010.

[60] S. Banerjee, C.-H. Liu, K. M. Ø. Jensen, P. Juhás, J. D. Lee, M. Tofanelli, C. J. Ackerson, C. B. Murray, and S. J. L. Billinge. Cluster-mining: an approach for determining core structures of metallic nanoparticles from atomic pair distribution function data. *Acta Crystallographica Section A: Foundations and Advances*, 76(1):24–31, January 2020.

[61] V. Petkov, S. Shastri, J.-W. Kim, S. Shan, J. Luo, J. Wu, and C.-J. Zhong. Application of differential resonant high-energy X-ray diffraction to three-dimensional structure studies of nanosized materials: A case study of Pt–Pd nanoalloy catalysts. *Acta Crystallographica Section A: Foundations and Advances*, 74(5):553–566, September 2018.

[62] Soham Banerjee, Chia-Hao Liu, Jennifer D. Lee, Anton Kovyakh, Viktoria Grasmik, Oleg Prymak, Christopher Koenigsmann, Haiqing Liu, Lei Wang, A. M. Milinda Abeykoon, Stanislaus S. Wong, Matthias Epple, Christopher B. Murray, and Simon J. L. Billinge. Improved Models for Metallic Nanoparticle Cores from Atomic Pair Distribution Function (PDF) Analysis. *The Journal of Physical Chemistry C*, 122(51):29498–29506, December 2018. Publisher: American Chemical Society.

[63] L. Yang, E. A. Culbertson, N. K. Thomas, H. T. Vuong, E. T. S. Kjær, K. M. Ø. Jensen, M. G. Tucker, and S. J. L. Billinge. A cloud platform for atomic pair distribution function analysis: PDFitc. *Acta Crystallographica Section A: Foundations and Advances*, 77(1):2–6, January 2021.

[64] Pablo D. Jadzinsky, Guillermo Calero, Christopher J. Ackerson, David A. Bushnell, and Roger D. Kornberg. Structure of a Thiol Monolayer-Protected Gold Nanoparticle at 1.1 Å Resolution. *Science*, 318(5849):430–433, October 2007.

[65] P. Juhás, D. M. Cherba, P. M. Duxbury, W. F. Punch, and S. J. L. Billinge. Ab initio determination of solid-state nanostructure. *Nature*, 440(7084):655–658, March 2006.

[66] Callum A. Young and Andrew L. Goodwin. Applications of pair distribution function methods to contemporary problems in materials chemistry. *Journal of Materials Chemistry*, 21(18):6464, 2011.

[67] Alexander N. Beecher, Xiaohao Yang, Joshua H. Palmer, Alexandra L. LaGrassa, Pavol Juhás, Simon J. L. Billinge, and Jonathan S. Owen. Atomic Structures and Gram Scale Synthesis of Three Tetrahedral Quantum Dots. *Journal of the American Chemical Society*, 136(30):10645–10653, July 2014.

[68] Jianwei Miao, Peter Ercius, and Simon J. L. Billinge. Atomic electron tomography: 3D structures without crystals. *Science*, 353(6306), September 2016.

[69] A. W. Castleman and S. N. Khanna. Clusters, Superatoms, and Building Blocks of New Materials. *J. Phys. Chem. C*, 113(7):2664–2675, February 2009.

[70] Arthur C. Reber and Shiv N. Khanna. Superatoms: Electronic and Geometric Effects on Reactivity. *Acc. Chem. Res.*, 50(2):255–263, February 2017.

[71] Anouck M. Champsaur, Alexandra Velian, Daniel W. Paley, Bonnie Choi, Xavier Roy, Michael L. Steigerwald, and Colin Nuckolls. Building Diatomic and Triatomic Superatom Molecules. *Nano Lett.*, 16(8):5273–5277, August 2016.

[72] Mingkui Wang, Alina M. Anghel, Benoît Marsan, Ngoc-Le Cevey Ha, Nuttapol Pootrakulchote, Shaik. M. Zakeeruddin, and Michael Grätzel. CoS Supersedes Pt as Efficient Electrocatalyst for Triiodide Reduction in Dye-Sensitized Solar Cells. *Journal of the American Chemical Society*, 131(44):15976–15977, November 2009.

[73] Yujie Sun, Chong Liu, David C. Grauer, Junko Yano, Jeffrey R. Long, Peidong Yang, and Christopher J. Chang. Electrodeposited Cobalt-Sulfide Catalyst for Electrochemical and Photoelectrochemical Hydrogen Generation from Water. *J. Am. Chem. Soc.*, 135(47):17699–17702, November 2013.

[74] Qinghong Wang, Lifang Jiao, Yan Han, Hongmei Du, Wenxiu Peng, Qingna Huan, Dawei Song, Yuchang Si, Yijing Wang, and Huatang Yuan. CoS_2 Hollow Spheres: Fabrication and Their Application in Lithium-Ion Batteries. *J. Phys. Chem. C*, 115(16):8300–8304, April 2011.

[75] Alexander P. Aydt, Boyu Qie, Andrew Pinkard, Long Yang, Qian Cheng, Simon J. L. Billinge, Yuan Yang, and Xavier Roy. Microporous Battery Electrodes from Molecular Cluster Precursors. *ACS Appl. Mater. Interfaces*, 11(12):11292–11297, March 2019.

[76] L. Yang, P. Juhás, M. W. Terban, M. G. Tucker, and S. J. L. Billinge. Structure-mining: Screening structure models by automated fitting to the atomic pair distribution function over large numbers of models. *Acta Cryst. A*, 76(3):395–409, May 2020.

[77] Sandeep Arya, Prerna Mahajan, Ramashanker Gupta, Ritu Srivastava, Naveen kumar Tailor, Soumitra Satapathi, R. Radhakrishnan Sumathi, Ram Datt, and Vinay Gupta. A comprehensive review on synthesis and applications of single crystal perovskite halides. *Progress in Solid State Chemistry*, 60:100286, December 2020.

[78] Lata Chouhan, Sushant Ghimire, Challapalli Subrahmanyam, Tsutomu Miyasaka, and Vasudevanpillai Biju. Synthesis, optoelectronic properties and applications of halide perovskites. *Chemical Society Reviews*, 49(10):2869–2885, May 2020.

[79] Joshua J. Choi, Xiaohao Yang, Zachariah M. Norman, Simon J. L. Billinge, and Jonathan S. Owen. Structure of Methylammonium Lead Iodide Within Mesoporous Titanium Dioxide: Active Material in High-Performance Perovskite Solar Cells. *Nano Letters*, 14(1):127–133, January 2014.

[80] Thomas M. Brenner, David A. Egger, Leeor Kronik, Gary Hodes, and David Cahen. Hybrid organic—inorganic perovskites: low-cost semiconductors with intriguing charge-transport properties. *Nature Reviews Materials*, 1(1):1–16, January 2016.

[81] Guan-Woo Kim and Annamaria Petrozza. Defect Tolerance and Intolerance in Metal-Halide Perovskites. *Advanced Energy Materials*, 10(37):2001959, 2020.

[82] Davide Raffaele Ceratti, Yevgeny Rakita, Llorenç Cremonesi, Ron Tenne, Vyacheslav Kalchenko, Michael Elbaum, Dan Oron, Marco Alberto Carlo Potenza, Gary Hodes, and David Cahen. Self-Healing Inside $APbBr_3$ Halide Perovskite Crystals. *Advanced Materials*, 30(10):1706273, 2018.

[83] Andrea Ciccioli and Alessandro Latini. Thermodynamics and the Intrinsic Stability of Lead Halide Perovskites $CH_3NH_3PbX_3$. *The Journal of Physical Chemistry Letters*, 9(13):3756–3765, July 2018.

[84] Yevgeny Rakita, Sidney R. Cohen, Nir Klein Kedem, Gary Hodes, and David Cahen. Mechanical properties of $APbX_3$ (A = Cs or CH_3NH_3; X = I or Br) perovskite single crystals. *MRS Communications*, 5(4):623–629, December 2015.

[85] Yevgeny Rakita, Igor Lubomirsky, and David Cahen. When defects become 'dynamic': halide perovskites: a new window on materials? *Materials Horizons*, 6(7):1297–1305, 2019.

[86] Ayala V. Cohen, David A. Egger, Andrew M. Rappe, and Leeor Kronik. Breakdown of the Static Picture of Defect Energetics in Halide Perovskites: The Case of the Br Vacancy in $CsPbBr_3$. *The Journal of Physical Chemistry Letters*, 10(16):4490–4498, August 2019.

[87] Richard J. Worhatch, HyunJeong Kim, Ian P. Swainson, André L. Yonkeu, and Simon J. L. Billinge. Study of Local Structure in Selected Organic–Inorganic Perovskites in the $Pm\bar{3}m$ Phase. *Chemistry of Materials*, 20(4):1272–1277, February 2008.

[88] Jin-Wook Lee, Seongrok Seo, Pronoy Nandi, Hyun Suk Jung, Nam-Gyu Park, and Hyunjung Shin. Dynamic structural property of organic-inorganic metal halide perovskite. *iScience*, 24(1):101959, January 2021.

[89] Omer Yaffe, Yinsheng Guo, Liang Z. Tan, David A. Egger, Trevor Hull, Constantinos C. Stoumpos, Fan Zheng, Tony F. Heinz, Leeor Kronik, Mercouri G. Kanatzidis, Jonathan S. Owen, Andrew M. Rappe, Marcos A. Pimenta, and Louis E. Brus. Local Polar Fluctuations in Lead Halide Perovskite Crystals. *Physical Review Letters*, 118(13):136001, March 2017.

[90] Miguel A. Pérez-Osorio, Rebecca L. Milot, Marina R. Filip, Jay B. Patel, Laura M. Herz, Michael B. Johnston, and Feliciano Giustino. Vibrational Properties of the Organic–Inorganic Halide Perovskite $CH_3NH_3PbI_3$ from Theory and Experiment: Factor Group Analysis, First-Principles Calculations, and Low-Temperature Infrared Spectra. *The Journal of Physical Chemistry C*, 119(46):25703–25718, November 2015.

[91] Tom Baikie, Nathan S. Barrow, Yanan Fang, Philip J. Keenan, Peter R. Slater, Ross O. Piltz, Matthias Gutmann, Subodh G. Mhaisalkar, and Tim J. White. A combined single crystal neutron/x-ray diffraction and solid-state nuclear magnetic resonance study of the hybrid perovskites $CH_3NH_3PbX_3$ (X = I, Br and Cl). *Journal of Materials Chemistry A*, 3(17), 2015.

[92] P. S. Whitfield, N. Herron, W. E. Guise, K. Page, Y. Q. Cheng, I. Milas, and M. K. Crawford. Structures, Phase Transitions and Tricritical Behavior of the Hybrid Perovskite Methyl Ammonium Lead Iodide. *Scientific Reports*, 6(1):35685, October 2016.

[93] Federica Bertolotti, Loredana Protesescu, Maksym V. Kovalenko, Sergii Yakunin, Antonio Cervellino, Simon J. L. Billinge, Maxwell W. Terban, Jan Skov Pedersen, Norberto Masciocchi, and Antonietta Guagliardi. Coherent Nanotwins and Dynamic Disorder in Cesium Lead Halide Perovskite Nanocrystals. *ACS Nano*, 11(4):3819–3831, April 2017.

[94] Anthony K. Cheetham, Thomas D. Bennett, François-Xavier Coudert, and Andrew L. Goodwin. Defects and disorder in metal organic frameworks. *Dalton Trans.*, 45:4113–4126, 2016.

[95] A. Schneemann, V. Bon, I. Schwedler, I. Senkovska, S. Kaskel, and R. A. Fischer. Flexible metal–organic frameworks. *Chem. Soc. Rev.*, 43:6062–6096, 2014.

[96] Karena W. Chapman, Peter J. Chupas, and Cameron J. Kepert. Selective recovery of dynamic guest structure, in a nanoporous Prussian Blue through *in situ* X-ray diffraction: A differential pair distribution function analysis. *Journal of the American Chemical Society*, 127(32):11232–11233, 2005.

[97] Nicholas C. Burtch, Samuel J. Baxter, Jurn Heinen, Ashley Bird, Andreas Schneemann, David Dubbeldam, and Angus P. Wilkinson. Negative thermal expansion design strategies in a diverse series of metal–organic frameworks. *Adv. Funct. Mater.*, 29(28):1904669, 2019.

[98] Thomas D. Bennett, Andrew L. Goodwin, Martin T. Dove, David A. Keen, Matthew G. Tucker, Emma R. Barney, Alan K. Soper, Erica G. Bithell, Jin-Chong Tan, and Anthony K. Cheetham. Structure and properties of an amorphous metal–organic framework. *Physical Review Letters*, 104(11):115503, 2010.

[99] David A. Keen and Thomas D. Bennett. Structural investigations of amorphous metal–organic frameworks formed via different routes. *Phys. Chem. Chem. Phys.*, 20:7857–7861, 2018.

[100] Thomas D. Bennett, Paul J. Saines, David A. Keen, Jin-Chong Tan, and Anthony K. Cheetham. Ball-milling-induced amorphization of zeolitic imidazolate frameworks (ZIFs) for the irreversible trapping of iodine. *Chemistry – A European Journal*, 19(22):7049–7055, 2013.

[101] Claudia Orellana-Tavra, Emma F. Baxter, Tian Tian, Thomas D. Bennett, Nigel K. H. Slater, Anthony K. Cheetham, and David Fairen-Jimenez. Amorphous metal–organic frameworks for drug delivery. *Chem. Commun.*, 51:13878–13881, 2015.

[102] Andy I. Nguyen, Kurt M. Van Allsburg, Maxwell W. Terban, Michal Bajdich, Julia Oktawiec, Micah S. Ziegler, James P. Dombrowski, K. V. Lakshmi, Walter S. Drisdell, Junko Yano, Simon J. L. Billinge, and T. Don Tilley. Stabilization of reactive Co_4O_4 cubane oxygen-evolution catalysts within porous frameworks. *PNAS*, 116(24):11630–11639, 2019.

[103] Romain Gaillac, Pluton Pullumbi, Kevin A. Beyer, Karena W. Chapman, David A. Keen, Thomas D. Bennett, and François-Xavier Coudert. Liquid metal–organic frameworks. *Nature Materials*, 16(11):1149–1154, 2017.

[104] Louis Longley, Sean M. Collins, Shichun Li, Glen J. Smales, Ilknur Erucar, Ang Qiao, Jingwei Hou, Cara M. Doherty, Aaron W. Thornton, Anita J. Hill, Xiao Yu, Nicholas J. Terrill, Andrew J. Smith, Seth M. Cohen, Paul A. Midgley, David A. Keen, Shane G. Telfer, and Thomas D. Bennett. Flux melting of metal–organic frameworks. *Chem. Sci.*, 10:3592–3601, 2019.

[105] Mengtan Liu, Ryan D. McGillicuddy, Hung Vuong, Songsheng Tao, Adam H. Slavney, Miguel I. Gonzalez, Simon J. L. Billinge, and Jarad A. Mason. Network-forming liquids from metal–bis(acetamide) frameworks with low melting temperatures. *Journal of the American Chemical Society*, 2021.

[106] Maxwell W. Terban, Debasis Banerjee, Sanjit Ghose, Bharat Medasani, Anil Shukla, Benjamin A. Legg, Yufan Zhou, Zihua Zhu, Maria L. Sushko, Jim J. De Yoreo, Jun Liu, Praveen K. Thallapally, and Simon J. L. Billinge. Early stage structural development of prototypical zeolitic imidazolate framework (ZIF) in solution. *Nanoscale*, 10:4291–4300, 2018.

[107] Hui Xu, Sanna Sommer, Nils Lau Nyborg Broge, Junkuo Gao, and Bo Brummerstedt. The chemistry of nucleation: *in situ* pair distribution function analysis of secondary building units during UiO-66 mof formation. *Chem. Eur.J.*, 25(8):2051–2058, 2019.

[108] Maxwell W. Terban, Sanjit K. Ghose, Anna M. Plonka, Diego Troya, Pavol Juhás, Robert E. Dinnebier, John J. Mahle, Wesley O. Gordon, and Anatoly I. Frenkel. Atomic resolution tracking of nerve-agent simulant decomposition and host metal–organic framework response in real space. *Communications Chemistry*, 4(2), 2021.

[109] Ines E. Collings, Matthew G. Tucker, David A. Keen, and Andrew L. Goodwin. Static disorder and local structure in zinc(ii) isonicotinate, a quartzlike metal–organic framework. *Z. Kristallogr.*, 227:313–320, 2012.

[110] Charlotte Koschnick, Robert Stäglich, Tanja Scholz, Maxwell W. Terban, Alberto von Mankowski, Gökcen Savasci, Florian Binder, Alexander Schökel, Martin Etter, Jürgen Nuss, Renée Siegel, Luzia S. Germann, Christian Ochsenfeld, Robert E. Dinnebier, Jürgen Senker, and Bettina V. Lotsch. Disorder and linker deficiency in porphyrinic Zr-MOFs: resolving the Zr_8O_6 cluster conundrum in PCN-221. *ChemRxiv*, https://doi.org/10.26434/chemrxiv.12918968.v1, 2020.

[111] Ana E. Platero-Prats, Andreas Mavrandonakis, Leighanne C. Gallington, Yangyang Liu, Joseph T. Hupp, Omar K. Farha, Christopher J. Cramer, and Karena W. Chapman. Structural transitions of the metal–oxide nodes within metal–organic frameworks: on the local structures of NU-1000 and UiO-66. *Journal of the American Chemical Society*, 138(12):4178–4185, 2016.

[112] Ana E. Platero-Prats, Aaron B. League, Varinia Bernales, Jingyun Ye, Leighanne C. Gallington, Aleksei Vjunov, Neil M. Schweitzer, Zhanyong Li, Jian Zheng, B. Layla Mehdi, Andrew J. Stevens, Alice Dohnalkova, Mahalingam Balasubramanian, Omar K. Farha, Joseph T. Hupp, Nigel D. Browning, John L. Fulton, Donald M. Camaioni, Johannes A. Lercher, Donald G.

Truhlar, Laura Gagliardi, Christopher J. Cramer, and Karena W. Chapman. Bridging zirconia nodes within a metal–organic framework via catalytic Ni-hydroxo clusters to form heterobimetallic nanowires. *Journal of the American Chemical Society*, 139(30):10410–10418, 2017.

[113] Timur Islamoglu, Zhijie Chen, Megan C. Wasson, Cassandra T. Buru, Kent O. Kirlikovali, Unjila Afrin, Mohammad Rasel Mian, and Omar K. Farha. Metal–organic frameworks against toxic chemicals. *Chemical Reviews*, 120(16), 2020.

[114] B. E. Warren. X-ray diffraction in random layer lattices. *Phys. Rev.*, 59:693–698, 1941.

[115] H. Y. Playford, T. F. Whale, B. J. Murray, M. G. Tucker, and C. G. Salzmann. Analysis of stacking disorder in ice I using pair distribution functions. *J. Appl. Cryst.*, 51(4):1211–1220, 2018.

[116] Alexander M. Pütz, Maxwell W. Terban, Sebastian Bette, Frederik Haase, Robert E. Dinnebier, and Bettina V. Lotsch. Total scattering reveals the hidden stacking disorder in a 2D covalent organic framework. *Chem. Sci.*, 11:12647–12654, 2020.

[117] Sebastian Bette, Tomohiro Takayama, Kentaro Kitagawa, Riku Takano, Hidenori Takagi, and Robert E. Dinnebier. Solution of the heavily stacking faulted crystal structure of the honeycomb iridate $H_3LiIr_2O_6$. *Dalton Trans.*, 46:15216–15227, 2017.

[118] Sebastian Bette, Tomohiro Takayama, Viola Duppel, Agnieszka Poulain, Hidenori Takagi, and Robert E. Dinnebier. Crystal structure and stacking faults in the layered honeycomb, delafossite-type materials $Ag_3LiIr_2O_6$ and $Ag_3LiRu_2O_6$. *Dalton Trans.*, 48:9250–9259, 2019.

[119] Daniel Scott Charles, Mikhail Feygenson, Katharine Page, Joerg Neuefeind, Wenqian Xu, and Xiaowei Tenga. Structural water engaged disordered vanadium oxide nanosheets for high capacity aqueous potassium-ion storage. *Nature Communications*, 8:15520, 2017.

[120] Hendrik Schlomberg, Julia Kröger, Gökcen Savasci, Maxwell W. Terban, Sebastian Bette, Igor Moudrakovski, Viola Duppel, Filip Podjaski, Renée Siegel, Jürgen Senker, Robert E. Dinnebier, Christian Ochsenfeld, and Bettina V. Lotsch. Structural insights into poly(heptazine imides): a light-storing carbon nitride material for dark photocatalysis. *Chem. Mater.*, 31:7478–7486, 2019.

[121] Christopher L. Farrow, D. Kwabena Bediako, Yogesh Surendranath, Daniel G. Nocera, and Simon J. L. Billinge. Intermediate-range structure of self-assembled cobalt-based oxygen evolving catalysts. *Journal of the American Chemical Society*, 135:6403–6406, 2013.

[122] Maxwell W. Terban, Chenyang Shi, Rita Silbernagel, Abraham Clearfield, and Simon J. L. Billinge. Local environment of terbium(iii) ions in layered nanocrystalline zirconium(iv) phosphonate–phosphate ion exchange materials. *Inorg. Chem.*, 56(15):8837–8846, 2017.

[123] Nicholas P. Funnell, Qiang Wang, Leigh Connor, Matthew G. Tucker, Dermot O'Hare, and Andrew L. Goodwin. Structural characterisation of a layered double hydroxide nanosheet. *Nanoscale*, 6:8032–8036, 2014.

[124] V. Petkov, S. J. L. Billinge, J. Heising, and M. G. Kanatzidis. Application of atomic pair distribution function analysis to materials with intrinsic disorder. three-dimensional structure of exfoliated-restacked WS_2: not just a random turbostratic assembly of layers. *Journal of the American Chemical Society*, 122:11571, 2000.

[125] Chenyang Shi, Majid Beidaghi, Michael Naguib, Olha Mashtalir, Yury Gogotsi, and Simon J. L. Billinge. Structure of nanocrystalline Ti_3C_2 MXene using atomic pair distribution function. *Phys. Rev. Lett.*, 112:125501, 2014.

[126] Peter C. Metz, Robert Koch, and Scott T. Misture. Differential evolution and markov chain monte carlo analyses of layer disorder in nanosheet ensembles using total scattering. *J. Appl. Cryst.*, 51:1437–1444, 2018.

[127] K. M. Ø. Jensen, A. B. Blichfeld, S. R. Bauers, S. R. Wood, E. Dooryhée, D. C. Johnson, B. B. Iversen, and S. J. L. Billinge. Demonstration of thin film pair distribution function analysis (tfPDF) for the study of local structure in amorphous and crystalline thin films. *IUCrJ*, 2(5):481–489, September 2015.

[128] Peter J. Chupas, Karena W. Chapman, and Peter L. Lee. Applications of an amorphous silicon-based area detector for high-resolution, high-sensitivity and fast time-resolved pair distribution function measurements. *Journal of Applied Crystallography*, 40(3):463–470, Jun 2007.

[129] Maxwell W. Terban, Matthew Johnson, Marco Di Michiel, and Simon J. L. Billinge. Detection and characterization of nanoparticles in suspension at low concentrations using the X-ray total scattering pair distribution function technique. *Nanoscale*, 7(12):5480–5487, March 2015.

[130] Private communication.

[131] Nathan Nakamura, Maxwell W. Terban, Simon J. L. Billinge, and B. Reeja-Jayan. Unlocking the structure of mixed amorphous-crystalline ceramic oxide films synthesized under low temperature electromagnetic excitation. *Journal of Materials Chemistry A*, 5(35):18434–18441, September 2017.

[132] Jeremy L. Hitt, Yuguang C. Li, Songsheng Tao, Zhifei Yan, Yue Gao, Simon J. L. Billinge, and Thomas E. Mallouk. A high throughput optical method for studying compositional effects in electrocatalysts for CO_2 reduction. *Nature Communications*, 12(1):1114, February 2021.

[133] A.-C. Dippel, M. Roelsgaard, U. Boettger, T. Schneller, O. Gutowski, and U. Ruett. Local atomic structure of thin and ultrathin films via rapid high-energy X-ray total scattering at grazing incidence. *IUCrJ*, 6(2):290–298, March 2019.

[134] Suzannah R. Wood, Keenan N. Woods, Paul N. Plassmeyer, David A. Marsh, Darren W. Johnson, Catherine J. Page, Kirsten M. Ø. Jensen, and David C. Johnson. Same Precursor, Two Different Products: Comparing the Structural Evolution of In–Ga–O "Gel-Derived" Powders and Solution-Cast Films Using Pair Distribution Function Analysis. *Journal of the American Chemical Society*, 139(15):5607–5613, 2017. PMID: 28328207.

[135] M. Roelsgaard, A.-C. Dippel, K. A. Borup, I. G. Nielsen, N. L. N. Broge, J. T. Röh, O. Gutowski, and B. B. Iversen. Time-resolved grazing-incidence pair distribution functions during deposition by radio-frequency magnetron sputtering. *IUCrJ*, 6(2):299–304, March 2019.

[136] Ann-Christin Dippel, Olof Gutowski, Lars Klemeyer, Ulrich Boettger, Fenja Berg, Theodor Schneller, Alexander Hardtdegen, Stephan Aussen, Susanne Hoffmann-Eifert, and Martin v Zimmermann. Evolution of short-range order in chemically and physically grown thin film bilayer structures for electronic applications. *Nanoscale*, 12(24):13103–13112, June 2020.

[137] Zizhou Gong and Simon J. L. Billinge. Atomic pair distribution functions (PDFs) from textured polycrystalline samples: fundamentals. *arXiv:1805.10342 [cond-mat]*, May 2018.

[138] W. Dmowski, C. Fan, M. L. Morrison, P. K. Liaw, and T. Egami. Structural changes in bulk metallic glass after annealing below the glass-transition temperature. *Materials Science and Engineering: A*, 471(1):125–129, December 2007.

[139] B. E. Warren, H. Krutter, and O. Morningstar. Fourier analysis of x-ray patterns of vitreous SiO_2 and B_2O_2. *Journal of the American Ceramic Society*, 19(1-12):202–206, 1936.

[140] J. H. Konnert and J. Karle. The computation of radial distribution functions for glassy materials. *Acta Crystallographica Section A: Crystal Physics, Diffraction, Theoretical and General Crystallography*, 29(6):702–710, November 1973.

[141] Yevgeny Rakita, James L. Hart, Partha Pratim Das, Stavros Nicolopoulos, Sina Shahrezaei, Suveen N. Mathaudhu, Mitra L. Taheri, and Simon J. L. Billing. Studying heterogeneities at the nanoscale with scanning nanostructure electron microscopy (SNEM). *Unpublished*.

[142] Morrel H. Cohen and David Turnbull. Molecular Transport in Liquids and Glasses. *The Journal of Chemical Physics*, 31(5):1164–1169, November 1959.

[143] T. Egami. Structural relaxation in amorphous $Fe_{40}Ni_{40}P_{14}B_6$ studied by energy dispersive X-ray diffraction. *Journal of Materials Science*, 13(12):2587–2599, December 1978.

[144] D. Srolovitz, T. Egami, and V. Vitek. Radial distribution function and structural relaxation in amorphous solids. *Physical Review B*, 24(12):6936–6944, December 1981.

[145] J. Kakinoki, Y. Komura, and T. Ino. Electron diffraction study of evaporated carbon films. *Acta Crystallographica*, 13(3):171–179, March 1960.

[146] A. M. Milinda Abeykoon, Christos D. Malliakas, Pavol Juhás, Emil S. Bozin, Mercouri G. Kanatzidis, and Simon J. L. Billinge. Quantitative nanostructure characterization using atomic pair distribution functions obtained from laboratory electron microscopes. *Zeitschrift für Kristallographie - Crystalline Materials*, 227(5):248–256, May 2012.

[147] Xiaoke Mu, Di Wang, Tao Feng, and Christian Kübel. Radial distribution function imaging by STEM diffraction: Phase mapping and analysis of heterogeneous nanostructured glasses. *Ultramicroscopy*, 168:1–6, September 2016.

[148] S. Y. Liu, Q. P. Cao, X. Mu, T. D. Xu, D. Wang, K. Ståhl, X. D. Wang, D. X. Zhang, C. Kübel, and J. Z. Jiang. Tracing intermediate phases during crystallization in a Ni–Zr metallic glass. *Acta Materialia*, 186:396–404, March 2020.

[149] Xiaoke Mu, Andrey Mazilkin, Christian Sprau, Alexander Colsmann, and Christian Kübel. Mapping structure and morphology of amorphous organic thin films by 4D-STEM pair distribution function analysis. *Microscopy*, 68(4):301–309, August 2019.

[150] Easo P. George, Dierk Raabe, and Robert O. Ritchie. High-entropy alloys. *Nature Reviews Materials*, 4(8):515–534, August 2019.

[151] James J. De Yoreo, Pupa U. P. A. Gilbert, Nico A. J. M. Sommerdijk, R. Lee Penn, Stephen Whitelam, Derk Joester, Hengzhong Zhang, Jeffrey D. Rimer, Alexandra Navrotsky, Jillian F. Banfield, Adam F. Wallace, F. Marc Michel, Fiona C. Meldrum, Helmut Cölfen, and Patricia M. Dove. Crystallization by particle attachment in synthetic, biogenic, and geologic environments. *Science*, 349(6247), July 2015.

[152] Govindhan Dhanaraj, Kullaiah Byrappa, Vishwanath Prasad, and Michael Dudley, editors. *Springer Handbook of Crystal Growth*. Springer Handbooks. Springer-Verlag, Berlin Heidelberg, 2010.

[153] Mikkel Juelsholt, Troels Lindahl Christiansen, and Kirsten M. Ø. Jensen. Mechanisms for Tungsten Oxide Nanoparticle Formation in Solvothermal Synthesis: From Polyoxometalates to Crystalline Materials. *The Journal of Physical Chemistry C*, 123(8):5110–5119, February 2019.

[154] Emil Indrea, Anca Peter, Danut T. Silipas, Simina Dreve, Ramona-Crina Suciu, Marcela Corina Rosu, Virginia Danciu, and Veronica Cosoveanu. Structural characterisation of binary SiO_2/TiO_2 nanoparticle aerogels by X-ray scattering. *Journal of Physics: Conference Series*, 182:012066, August 2009.

[155] Peter J. Chupas, Karena W. Chapman, Guy Jennings, Peter L. Lee, and Clare P. Grey. Watching Nanoparticles Grow: The Mechanism and Kinetics for the Formation of TiO_2-Supported Platinum Nanoparticles. *Journal of the American Chemical Society*, 129(45):13822–13824, November 2007.

[156] Margarita Rekhtina, Alessandro Dal Pozzo, Dragos Stoian, Andac Armutlulu, Felix Donat, Maria V. Blanco, Zhu-Jun Wang, Marc-Georg Willinger, Alexey Fedorov, Paula M. Abdala, and Christoph R. Müller. Effect of molten sodium nitrate on the decomposition pathways of hydrated magnesium hydroxycarbonate to magnesium oxide probed by *in situ* total scattering. *Nanoscale*, 12(31):16462–16473, August 2020.

[157] Kirsten M. Ø. Jensen, Mogens Christensen, Pavol Juhás, Christoffer Tyrsted, Espen D. Bøjesen, Nina Lock, Simon J. L. Billinge, and Bo B. Iversen. Revealing the Mechanisms behind SnO_2 Nanoparticle Formation and Growth during Hydrothermal Synthesis: An *In Situ* Total Scattering Study. *Journal of the American Chemical Society*, 134(15):6785–6792, April 2012.

[158] Christoffer Tyrsted, Kirsten Marie Ørnsbjerg Jensen, Espen Drath Bøjesen, Nina Lock, Mogens Christensen, Simon J. L. Billinge, and Bo Brummerstedt Iversen. Understanding the Formation and Evolution of Ceria Nanoparticles Under Hydrothermal Conditions. *Angewandte Chemie International Edition*, 51(36):9030–9033, 2012.

[159] Christoffer Tyrsted, Brian Richard Pauw, Kirsten Marie Ørnsbjerg Jensen, Jacob Becker, Mogens Christensen, and Bo Brummerstedt Iversen. Watching Nanoparticles Form: An *In Situ* (Small-/Wide-Angle X-ray Scattering/Total Scattering) Study of the Growth of Yttria-Stabilised Zirconia in Supercritical Fluids. *Chemistry: A European Journal*, 18(18):5759–5766, April 2012.

[160] Kirsten M. Ø. Jensen, Mogens Christensen, Haraldur P. Gunnlaugsson, Nina Lock, Espen D. Bøjesen, Thomas Proffen, and Bo B. Iversen. Defects in Hydrothermally Synthesized $LiFePO_4$ and $LiFe_{1-x}Mn_xPO_4$ Cathode Materials. *Chemistry of Materials*, 25(11):2282–2290, June 2013.

[161] Kirsten M.Ø. Jensen, Christoffer Tyrsted, Martin Bremholm, and Bo B. Iversen. *In Situ* Studies of Solvothermal Synthesis of Energy Materials. *ChemSusChem*, 7(6):1594–1611, June 2014.

[162] Kirsten M. Ø. Jensen, Henrik L. Andersen, Christoffer Tyrsted, Espen D. Bøjesen, Ann-Christin Dippel, Nina Lock, Simon J. L. Billinge, Bo B. Iversen, and Mogens Christensen. Mechanisms for Iron Oxide Formation under Hydrothermal Conditions: An *In Situ* Total Scattering Study. *ACS Nano*, 8(10):10704–10714, October 2014.

[163] Dipankar Saha, Kirsten M. Ø. Jensen, Christoffer Tyrsted, Espen D. Bøjesen, Aref Hasen Mamakhel, Ann-Christin Dippel, Mogens Christensen, and Bo B. Iversen. *In Situ* Total X-Ray Scattering Study of WO_3 Nanoparticle Formation under Hydrothermal Conditions. *Angewandte Chemie International Edition*, 53(14):3667–3670, 2014.

[164] Espen D. Bøjesen, Kirsten M. Ø. Jensen, Christoffer Tyrsted, Aref Mamakhel, Henrik L. Andersen, Hazel Reardon, Jacques Chevalier, Ann-Christin Dippel, and Bo B. Iversen. The chemistry of $ZnWO_4$ nanoparticle formation. *Chemical Science*, 7(10):6394–6406, September 2016.

[165] Steinar Birgisson, Dipankar Saha, and Bo B. Iversen. Formation Mechanisms of Nanocrystalline MnO_2 Polymorphs under Hydrothermal Conditions. *Crystal Growth & Design*, 18(2):827–838, February 2018.

[166] Satoshi Tominaka, Hiroki Yamada, Satoshi Hiroi, Saori I. Kawaguchi, and Koji Ohara. Lepidocrocite-Type Titanate Formation from Isostructural Prestructures under Hydrothermal Reactions: Observation by Synchrotron X-ray Total Scattering Analyses. *ACS Omega*, 3(8):8874–8881, August 2018.

[167] Nils L. N. Broge, Frederik Søndergaard Pedersen, Sanna Sommer, and Bo B. Iversen. Formation Mechanism of Epitaxial Palladium-Platinum Core-Shell Nanocatalysts in a One-Step Supercritical Synthesis. *Advanced Functional Materials*, 29(31):1902214, 2019.

[168] Hiroki Yamada, Satoshi Tominaka, Koji Ohara, Zhendong Liu, Tatsuya Okubo, and Toru Wakihara. Structural Evolution of Amorphous Precursors toward Crystalline Zeolites Visualized by an *In Situ* X-ray Pair Distribution Function Approach. *The Journal of Physical Chemistry C*, 123(46):28419–28426, November 2019.

[169] Matthew E. Potter, Mark E. Light, Daniel J.M. Irving, Alice E. Oakley, Stephanie Chapman, Philip Chater, Geoff Cutts, Andrew Watts, Michael Wharmby, Bart D. Vandegehuchte, Moritz W. Schreiber, and Robert Raja. Exploring the origins of crystallisation kinetics in hierarchical materials using *in situ* X-ray diffraction and pair distribution function analysis. *Physical Chemistry Chemical Physics*, 22(34):18860–18867, 2020.

[170] Ola G. Grendal, Inger-Emma Nylund, Anders B. Blichfeld, Satoshi Tominaka, Koji Ohara, Sverre M. Selbach, Tor Grande, and Mari-Ann Einarsrud. Controlled Growth of $Sr_xBa_{1-x}Nb_2O_6$ Hopper- and Cube-Shaped Nanostructures by Hydrothermal Synthesis. *Chemistry: A European Journal*, 26(42):9348–9355, July 2020.

[171] Sanna Sommer, Espen D. Bøjesen, Hazel Reardon, and Bo B. Iversen. Atomic Scale Design of Spinel $ZnAl_2O_4$ Nanocrystal Synthesis. *Crystal Growth & Design*, 20(3):1789–1799, March 2020.

[172] Benjamin A. Frandsen, Xiaohao Yang, and Simon J. L. Billinge. Magnetic pair distribution function analysis of local magnetic correlations. *Acta Crystallogr. A*, 70(1):3–11, 2014.

[173] Benjamin A. Frandsen and Simon J. L. Billinge. Magnetic structure determination from the magnetic pair distribution function (mPDF): ground state of MnO. *Acta Crystallogr. A*, 71(3):325–334, 2015.

[174] Benjamin A. Frandsen, Emil S. Bozin, Eleni Aza, Antonio Fernández Martínez, Mikhail Feygenson, Katharine Page, and Alexandros Lappas. Nanoscale degeneracy lifting in a geometrically frustrated antiferromagnet. *Phys. Rev. B*, 101:024423, Jan 2020.

[175] xPDFsuite - an easy to use end-to-end software solution for atomic pair distribution function analysis with x-rays. https://www.diffpy.org/products/xPDFsuite.html.

[176] Lauri Himanen, Amber Geurts, Adam Stuart Foster, and Patrick Rinke. Data-Driven Materials Science: Status, Challenges, and Perspectives. *Advanced Science*, 6(21):1900808, 2019.

[177] C.-H. Liu, Y. Tao, D. Hsu, Q. Du, and S. J. L. Billinge. Using a machine learning approach to determine the space group of a structure from the atomic pair distribution function. *Acta Cryst. A*, 75(4):633–643, July 2019.

[178] A. Gilad Kusne, Heshan Yu, Changming Wu, Huairuo Zhang, Jason Hattrick-Simpers, Brian DeCost, Suchismita Sarker, Corey Oses, Cormac Toher, Stefano Curtarolo, Albert V. Davydov, Ritesh Agarwal, Leonid A. Bendersky, Mo Li, Apurva Mehta, and Ichiro Takeuchi. On-the-fly closed-loop materials discovery via Bayesian active learning. *Nature Communications*, 11(1):5966, November 2020.

[179] Yevgeny Rakita, Daniel O'Nolan, Rebecca D. McAuliffe, Gabriel M. Veith, Peter J. Chupas, Simon J. L. Billinge, and Karena W. Chapman. Active Reaction Control of Cu Redox State Based on Real-Time Feedback from *In Situ* Synchrotron Measurements. *Journal of the American Chemical Society*, 142(44):18758–18762, November 2020.

[180] Bluesky Project. https://blueskyproject.io/.

[181] Songsheng Tao. PDFstream: The configs analysis toolbox for the study on pair distribution function (PDF). https://github.com/xpdAcq/pdfstream.

[182] Christopher Right. SHED. *unpublished*, 2021.

[183] Nathan Nakamura, Laisuo Su, Jianming Bai, Sanjit Ghose, and B. Reeja-Jayan. *In situ* synchrotron pair distribution function analysis to monitor synthetic pathways under electromagnetic excitation. *Journal of Materials Chemistry A*, 8(31):15909–15918, August 2020.

[184] Hui Xu, Sanna Sommer, Nils Lau Nyborg Broge, Junkuo Gao, and Bo Brummerstedt Iversen. The Chemistry of Nucleation: *In Situ* Pair Distribution Function Analysis of Secondary Building Units During UiO-66 MOF Formation. *Chemistry: A European Journal*, 25(8):2051–2058, February 2019.

[185] Antoine E. Morandeau and Claire E. White. *In situ* X-ray pair distribution function analysis of accelerated carbonation of a synthetic calcium–silicate–hydrate gel. *Journal of Materials Chemistry A*, 3(16):8597–8605, April 2015.

[186] Simon D. M. Jacques, Marco Di Michiel, Simon A. J. Kimber, Xiaohao Yang, Robert J. Cernik, Andrew M. Beale, and Simon J. L. Billinge. Pair distribution function computed tomography. *Nature Communications*, 4(1):2536, September 2013.

[187] Kirsten M. Ø. Jensen, Xiaohao Yang, Josefa Vidal Laveda, Wolfgang G. Zeier, Kimberly A. See, Marco Di Michiel, Brent C. Melot, Serena A. Corr, and Simon J. L. Billinge. X-Ray Diffraction Computed Tomography for Structural Analysis of Electrode Materials in Batteries. *Journal of The Electrochemical Society*, 162(7):A1310, April 2015.

[188] James J. De Yoreo. *In-situ* liquid phase TEM observations of nucleation and growth processes. *Progress in Crystal Growth and Characterization of Materials*, 62(2):69–88, June 2016.